Ore Geology Reviews 177 (2025) 106466

Contents lists available at ScienceDirect

Ore Geology Reviews

journal homepage: www.elsevier.com/locate/oregeorev

Scandium distribution in the Bayan Obo REE-Nb-Fe deposit, China: A multi-scale geochemical perspective

Shuang-Liang Liu [a,b,c], Xuan Liu [c], Hong-Rui Fan [b,d,e,*], Alan R Butcher [c,f], Yann Lahaye [c], Radoslaw M. Michallik [c], Ester M. Jolis [c], Sari Lukkari [c], Kui-Feng Yang [b,d], Qi-Wei Wang [e], Zheng-Jie Qiu [b,d], Hai-Dong She [b,d]

[a] Deep Space Exploration Lab, Hefei 230088, PR China
[b] State Key Laboratory of Lithospheric and Environmental Coevolution, Institute of Geology and Geophysics, Chinese Academy of Sciences, Beijing 100029, PR China
[c] Geological Survey of Finland, P.O. Box 96, FI-02151 Espoo, Finland
[d] College of Earth and Planetary Sciences, University of Chinese Academy of Sciences, Beijing 100049, PR China
[e] State Key Laboratory of Baiyunobo Rare Earth Resource Researches and Comprehensive Utilization, Baotou Research Institute of Rare Earths, Baotou 014030, PR China
[f] Hafren Scientific Ltd, Welshpool, UK

ARTICLE INFO

Keywords:
Scandium
Thortveitite
Jervisite
Bazzite
Carbonatite
Bayan Obo

ABSTRACT

Scandium (Sc) is a dispersed element in average continental crust but can accumulate in carbonatite systems. In the Bayan Obo carbonatite deposit, China, substantial Sc_2O_3 resources have been estimated; however, the occurrence and spatial distribution of Sc remain poorly understood, impeding efforts to explore and extract these resources. This study presents novel results of geochemical, mineral and textural mapping from 270 systematically collected field samples and 13 representative laboratory samples, revealing the Sc distribution at various scales, from deposit down to mineral, within this complex carbonatite system.

Whole-rock analyses identified Sc anomalies (over 100 ppm) along the lithological contacts between the ore-hosting dolomite intrusion and the surrounding slate/schist. The banded/massive ores and vein-type ores exhibit variable yet relatively high Sc contents, ranging from 2 to 378 ppm (average 67.6 ppm) and 91 to 273 ppm (average 153 ppm), respectively. In contrast, slate/schist shows lower Sc levels (1–218 ppm, average 38.2 ppm), while the ore-hosting dolomite has consistently medium to low Sc contents (17–77 ppm, average 34.0 ppm). Micro-scale analyses reveal that aegirine and Na-amphibole are common Sc carriers in all rock types except slate/schist, in which mica and ilmenite are the major Sc-bearing minerals. Sc-rich domains (over 0.3 wt% Sc_2O_3) are detected in polished thin sections, in which three individual Sc minerals, i.e., thortveitite, aegirine-jervisite solid solution, and bazzite, are documented for the first time in this deposit. Variations in chemical composition and microtexture in these Sc minerals indicate a multi-stage Sc mineralization process. These findings suggest that hydrothermal alteration is the primary mechanism for Sc enrichment in this carbonatite system, laying a solid foundation for future resource utilization of the Bayan Obo deposit.

1. Introduction

Scandium (Sc) has many uses in high-tech and clean energy industries, and now is considered a critical metal by many countries (Critical Minerals Office, 2023; European Commission, 2023; USGS, 2024). It is widely used in Sc-Al alloys, solid oxide fuel cells, electronics, lasers, and lighting to innovate and enhance product performance and properties (Langan and Dorin, 2023; Phoung et al., 2023). Up until now, the production and consumption of Sc remains low (30–40 t/yr), largely due to a lack of global economic resources and industrially efficient extraction techniques. The short in supply has resulted in high market prices of ~ 269 $/g for Sc, about three times higher than that of gold, and has made scandium a topical research topic worldwide (Williams-Jones and Vasyukova, 2018; Halkoaho et al., 2020; Zhou et al., 2020, 2022; Hreus, et al., 2021; Wang et al., 2021, 2022b; Beland and Williams-Jones, 2023; Liu et al., 2023; USGS, 2024).

* Corresponding author.
E-mail address: fanhr@mail.iggcas.ac.cn (H.-R. Fan).

https://doi.org/10.1016/j.oregeorev.2025.106466
Received 30 November 2024; Received in revised form 15 January 2025; Accepted 17 January 2025
Available online 20 January 2025

Scandium is often considered a member of the rare earth group, even though its geochemical properties are quite distinctive compared to lanthanides (Samon and Chassé, 2016). It rarely forms individual Sc deposits, even though there are 23 known individual Sc minerals. Instead, it is dispersed within the Earth's crust, and commonly substitutes high field strength elements (HFSE) and Fe-Mg in minerals, such as Nb-Ta-Ti-Fe oxides (Siegfried et al., 2018) and ferromagnesium silicates (e.g., clinopyroxene; Williams-Jones and Vasyukova, 2018). In general, the Sc speciation varies according to deposit type, as follows: adsorbed Sc on goethite in the lateritic deposits (Chassé et al., 2016); heterogeneously distributed trace Sc in kinetically controlled diopside of magma-type deposits (Wang et al., 2022b); and Sc within zinnwaldite and HFSE minerals in greisen-type deposits (Hreus et al., 2021). Therefore, clarifying the distribution of scandium resources is the basis of Sc exploration and research.

Although Sc generally occurs in low concentrations in common minerals and lithologies, it can occasionally achieve moderately large quantities in carbonatite systems, such as the Elk Creek (America, 2400 t; Verbaan et al., 2018), Fen (Norway, existing thortveitite; Amli, 1977), Kovdor (Russia, 420 t, Tolstov and Gunin, 2001; Kalashnikov et al., 2016), Oka (Canada; Eby, 1973), and Tomtor (Russia, 39000 t, 390 ppm; Lapin et al., 2016). In general, the formation of carbonatite REE deposits

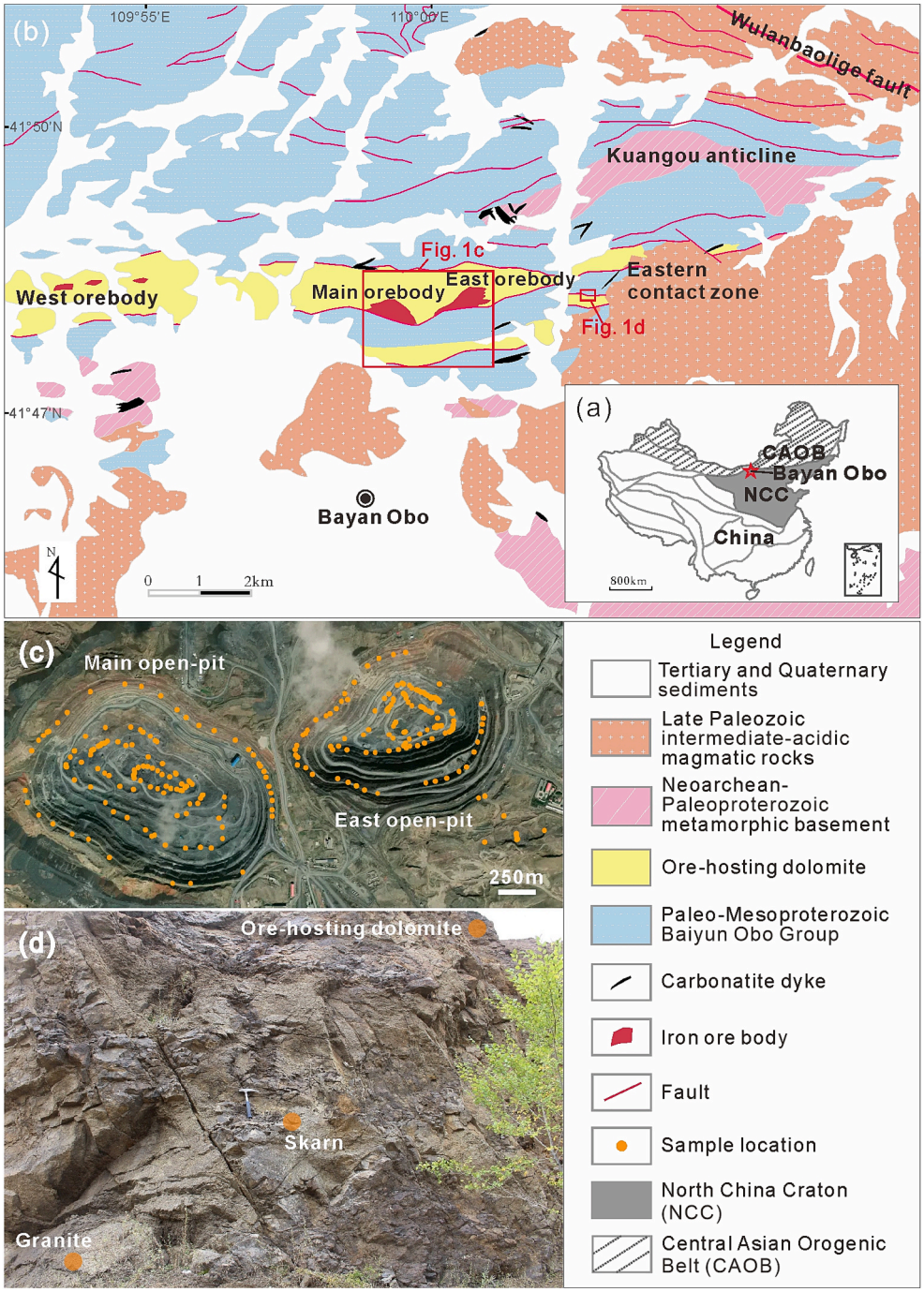

Fig. 1. (a) Simplified map of China, showing the locations of North China Craton and the Bayan Obo deposit. (b) Geological map of Bayan Obo deposit (Modified from Fan et al., 2022). (c) The top view of the Main and East open pits, with the sample locations marked as orange dots. (d) The section outcrop of the sample location of the east contact zone.

normally involves magmatic metal pre-enrichment, followed by hydrothermal remobilization and mineralization (Anenburg et al., 2021; Yaxley et al., 2022; Chen, et al., 2024). Experimental petrology and simulation calculations of scandium's distribution coefficient in magma differentiation and the migration of Sc complexes in fluids, have shown that both magmatic (especially hydrous carbonatite-mafic magmas) and hydrothermal (especially fluorine-rich fluids) processes can facilitate Sc dissolution and transport (Shchekina and Gramenitskii, 2008; Martin et al., 2013; Wang et al., 2022a). However, the enrichment characteristics of Sc in the carbonatite system are still unclear, and the relative contribution of magmatic and hydrothermal processes remains elusive.

The Bayan Obo REE-Nb-Fe carbonatite deposit is considered the largest source for future global Sc supply, with an estimated 140,000t @ 100 ppm (Ma, 2012; Williams-Jones and Vasyukova, 2018). It has been interpreted to have undergone both magmatic and multiple fluid-overprinting processes, ranging from early alkali metasomatism to post-depositional hydrothermal and thermal modifications (Smith et al., 2015; Yang et al., 2017; Li et al., 2021b; She et al., 2023).

Previous major element analyses of Sc in tailings at Bayan Obo found that Sc was enriched in some aegirine and Nb-bearing minerals

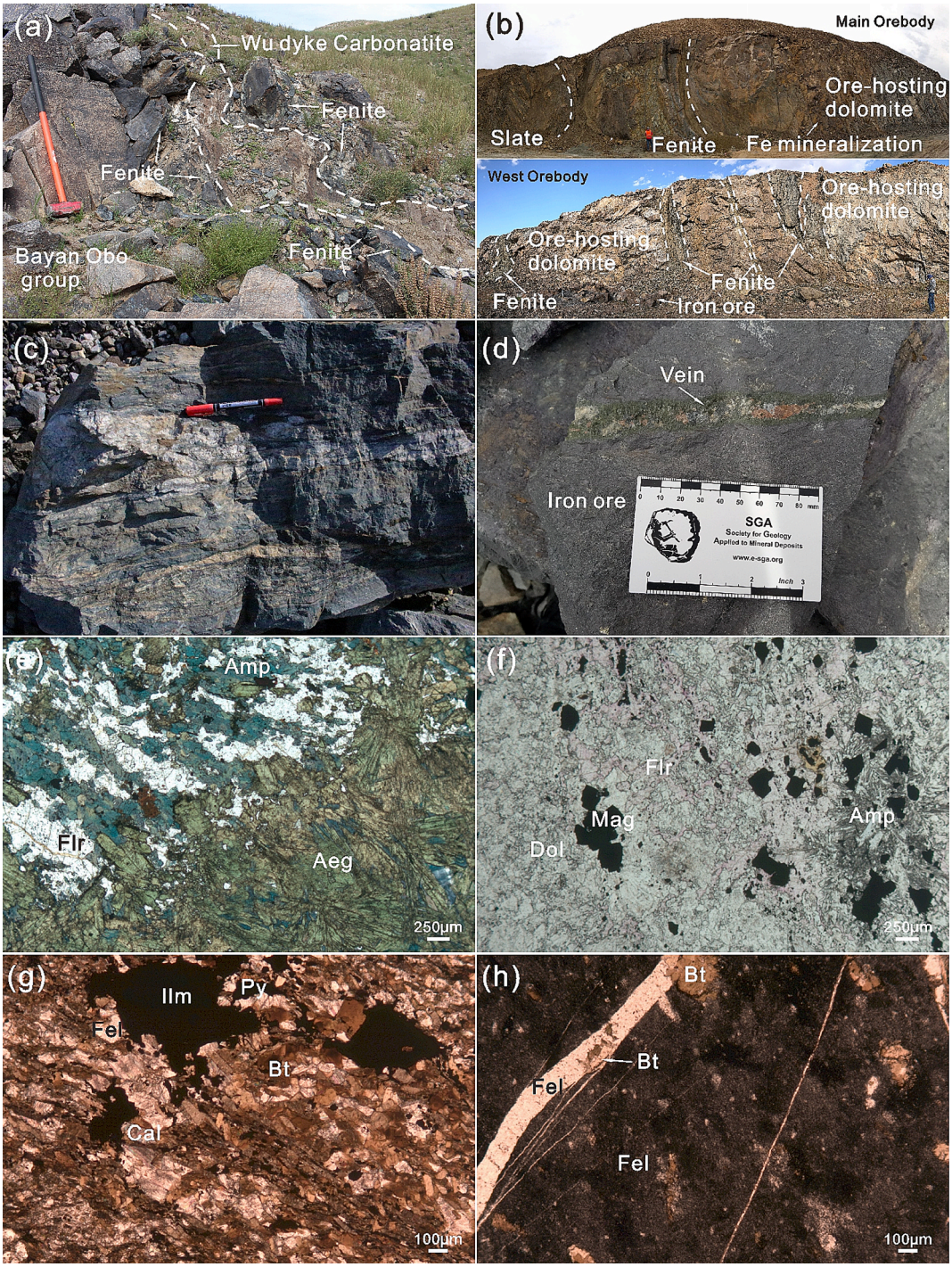

Fig. 2. (a) The outcrop of carbonatite dyke and surrounding alkali alteration. (b) The profile of Main and West orebody. (c) The typical ore rock of Bayan Obo deposit, sampled from the Main orebody. (d) The typical vein-type ores. (e-h) The microscopic view of banded/massive ores (e), ore-hosting dolomite (f), high-Sc slate/schist (g), low-Sc slate/schist (h).

(Shimazaki et al., 2008; Ma, 2012; Yang et al., 2022). However, little work has been previously carried out to understand the distribution of Sc within the *in-situ* ore zones. To fill this gap in knowledge, we systematically collected samples from the deposit, and investigated them in detail using various petrographic and geochemical techniques at different scales, with the objective of revealing the occurrence and distribution of Sc at Bayan Obo, as well as the enrichment processes that took place. We hope that this study will provide new information for all those interested in the Sc enrichment characteristics within carbonatite systems.

2. Geological setting

The Bayan Obo deposit (109°58′ E, 41°48′N) is located on the northern margin of the North China Craton (NCC), which is bounded by the Central Asia Orogenic Belt (CAOB) to the north and Qingling-Dabie-Sulu orogen to the south (Fig. 1a).

The region mainly consists of Neoarchean to Paleoproterozoic metamorphic basement rocks, Paleoproterozoic to Mesoproterozoic Bayan Obo Group cover, ore-hosting dolomite, carbonatite dykes, and Paleozoic granitoids (Fig. 1b). The basement rocks comprise granitic-gneiss, and granodiorite (around 2588–1890 Ma; Fan et al., 2016), distributed in the Kuangou fault region and south of the mining area. The Bayan Obo Group, exposed in the deposit, is a series of low-grade metamorphic sedimentary rocks, including arkosic quartzite, conglomerate, sandstone, limestone, slate, and interbedded slate and schist. These *meta*-sedimentary rocks have undergone intense deformation, resulting in tight folding (Ke et al., 2021; Fan et al., 2022). The ore-hosting dolomite was originally classified as a part of the Bayan Obo Group and named as the H8 unit. However, recent works indicated that the ore-hosting dolomite was an igneous dolomitic carbonatite rather than sedimentary carbonate (Chen et al., 2020; Kuebler et al., 2020; Tang et al., 2021; Fan et al., 2022; Yang et al., 2023a; Li et al., 2024). Radiometric dating suggested that the ore-hosting dolomite formed in the Mesoproterozoic (zircon Th-Pb age 1301 ± 12 Ma, Zhang et al., 2017b; 1317 ± 140 Ma, apatite Sm-Nd, Yang et al., 2019; hydrothermal zircon Th-Pb 1297 ± 13 Ma, Li et al., 2021a). The Palaeozoic granitoids consist of granodiorite, monzogranite, and biotite granite (zircon U-Pb 281–262 Ma), formed synchronously with the plate subduction during the closure of the Paleo-Asian Ocean (Fan et al., 2009). They are mainly exposed in the south and east of the mining area (named Eastern Contact Zone), generating skarns where in contact with ore-hosting dolomite (Fan et al., 2004; Zhang et al., 2017a). Over 100 carbonatite dikes intruded into the Bayan Obo Group and basement rocks, causing fenitization in the surrounding rocks (Fig. 2a; Liu et al., 2018). Geochemical and geochronological studies indicate that these dykes are genetically related to ore-hosting dolomite and are divided into ferroan, magnesian, and calcic varieties (Ren et al., 1994; Le Maitre, 2002; Le Bas et al., 2007; Fan et al., 2014; Yang et al., 2019).

As mentioned above, the Bayan Obo deposit is an extreme geological entity, containing around 333 Mt REE_2O_3 at 2 wt% (Fan et al., 2022). It also contains significant resources of Nb (2.16 Mt at 0.13 wt% Nb_2O_5) and Fe (>1500 Mt at 35 wt%) (Drew et al., 1990, Bai et al., 1996). In addition, significant Sc_2O_3 resources have been estimated at about 0.14 Mt with an average grade of 100 ppm (Ma et al., 2012; Williams-Jones and Vasyukova, 2018). Currently, the mined ore minerals are magnetite/hematite for iron and monazite/REE-fluorcarbonate for REE resources, with aeschynite, columbite, ilmenorutile, pyrochlore, fergusonite, and baotite for Nb (Fan et al., 2016; Hou et al., 2023; Ren et al., 2023). The three largest orebodies (defined by Fe tonnage) in Bayan Obo are named the Main, East, and West orebodies, located in the Main, East and West open-pits, respectively (Fig. 1). The East and Main orebodies mainly occur between the boundary of ore-hosting dolomite and Bayan Obo Group slate/schist (Fig. 2b). The West orebody is located mainly in the massive dolomitic carbonatite, with some slate/schist included (Fig. 2b).

This deposit is thought to have originally formed through carbonatite magmatism and a reaction of REE/Na-F-rich hydrothermal fluids with surrounding rocks (Bayan Obo Group and metamorphic basement rocks; Fig. 2a) at ca. 1.3 Ga, and then underwent two discrete episodes of post-ore formation hydrothermal activity at ~ 430 Ma and ~ 270 Ma (Fan et al., 2016; Zhang et al., 2017b; Li et al., 2021b; Yu et al., 2024). Ore zones commonly show heterogeneously banded structures defined by irregular bands of magnetite, fluorite, REE minerals (mainly monazite and bastnäsite), apatite, aegirine, and Na-amphibole. Some thicker bands as massive ores are also present (Fig. 2c, 2e-f). Both can be crosscut by hydrothermal veins of coarse-grained aegirine, calcite, fluorite, REE-fluorcarbonate (e.g., monazite, bastnäsite, parasite etc.), phlogopite, pyrite, and aeschynite (Fig. 2d). Because of the intensive post-ore formation metamorphic and metasomatic overprints on the originally mineralization, banded/massive type ores generally exhibit a wide age range of ages, ca. 1300–260 Ma with two peaks at ca. 450–400 Ma, and ca. 280–260 Ma (Li et al., 2021b), while the vein-type ores typically only have an age of ~ 440 Ma (sulfide Re-Os age, Liu et al., 2004; Hu et al., 2009).

3. Sampling and analytical methods

3.1. Sampling strategy

The Main and East open-pits were selected as the main sampling areas, based on geology and accessibility. A total of 265 samples were collected, comprising 258 samples of dolomite, banded/massive ores covering different rock types from the working platforms (Fig. 1c), as well as 7 vein-type ores from ore surrounding dumps. In addition, 5 samples were collected from the Eastern Contact Zone to assess the influence of the granitoid intrusion (Fig. 1d). All samples were analyzed for whole-rock major, minor and trace elements.

For in-depth investigations, representative samples were selected using the following the criteria: must cover all of the main rock types present at Bayan Obo mines; including both Main and East open pits; covering the range of whole-rock Sc contents of each rock type; including the most common mineral association of each rock type. Finally, 13 samples, including 3 dolomites, 4 alteration ores, 3 slates, and 3 vein-type ores, were selected for further thin-section mineral and texture mapping, as well as in-situ laser-based analyses (Fig. 3a; Table 1). All samples were divided into two parts, with one part for making thin sections and the other for whole-rock analysis.

3.2. Whole rock trace element analysis

The whole-rock trace elements were analyzed at the ALS Minerals, Guangzhou, China. Samples were first crushed using a hardened steel jaw crusher such that 70 % of the resulting fragments passed through a 2-mm screen size. Subsequently, these fragments were then powdered in an agate ball mill until > 85 % of them passed a 75-μm screen size. Trace elements, including REEs, were determined using lithium metaborate fusion digestion and ICP-MS, following ALS Geochemistry method ME-MS81h for high-REE-contents samples (relative deviation and error < 7 %) and ME-MS81 for normal samples (relative deviation and error < 10 %). Additionally, Be, Sc, Zn, Li, and Pb were determined by four-acid digestion followed by ICP-MS, adhering to ALS Geochemistry method ME-MS61r (relative deviation and error < 10 %).

3.3. Scanning micro-XRF and mineral identification

The first micro-geochemical and mineral investigations for locating Sc minerals were performed using a scanning micro-X-ray fluorescence (μ-XRF) M4 Tornado system, fitted with Bruker AMICS mineral analysis software, at the Geological Survey of Finland (GTK). The instrument was equipped with an Rh X-ray 30-Watt Rh anode target, two simultaneously operating 30 mm^2 XFlash® silicon drift detectors (SDDs) with an energy

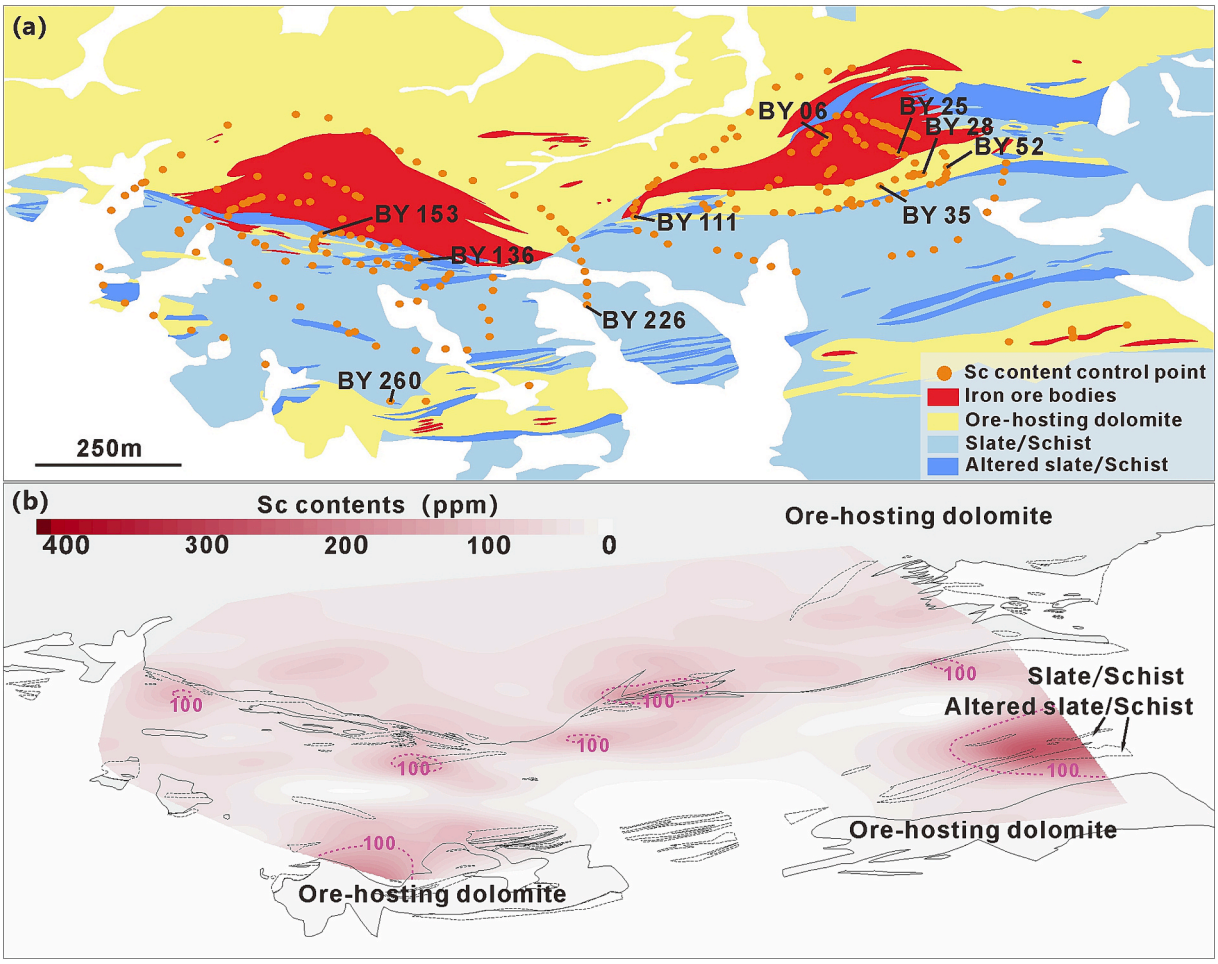

Fig. 3. The spatial comparison of whole-rock Sc contents distribution and major rock type in the main and east ore bodies of the Bayan Obo deposit. (a) Geology map of main and east mines with the representative samples named. (b) Corresponding whole-rock Sc contents distribution with the 100 ppm contours marked.

resolution of < 145 eV at 275 kcps (measured on MnKα). The Rh X-ray source was performed under maximum energy settings of 50 kV and a beam current of 600 μA. The beam was focused by a polycapillary lens on a fixed spot size of 20 μm under 2 mbar vacuum. The samples were mapped in separate runs using a step size of 20 μm and a pixel dwell time of 20 ms/pixel. The qualitative elemental maps were generated using the Bruker M4 software.

The mineral identification and characterizations were conducted using the Advanced Mineral Identification and Characterization System (AMICS) software. This software enabled mineral identification using μ-XRF datasets, where the collected X-ray spectral data underwent evaluation and comparison with a reference list of known mineral spectra. The process employed $\chi 2$ fingerprinting optimal mineral classification. Further refinement of mineral classification involved various clustering techniques and/or manual data reduction and evaluation of XRF spectral attributes, with data reclassification performed as necessary to address unclassified X-ray points (unknowns) (Bruker, 2018). The outcome of this procedure was a mineral-class map assigning a single or specific mineral mixture label to each pixel. This map facilitated the quantification of mineral properties such as modal abundance, grain size, and mineral association.

3.4. Back-scattered electron images and electron micro-probe analysis

Areas of interest within the thin sections were then imaged and analysed using a Scanning Electron Microscope, model Hitachi SU3900, equipped with an Oxford Instruments EDS-spectrometer X-Max 20 mm^2 (SDD).

Spot analysis and quantified wavelength-dispersive spectrometry (WDS) analysis was obtained with a JEOL JXA-iHP200F Hyperprobe field-emission electron microprobe analyzer (FEG-EMPA), also at GTK. Accelerating voltage and beam current were set to 15 kV and 20nA for the spot measurements. A defocused beam diameter set to 5 μm was used and for apatite set to 10 μm. Test measurements were performed to ensure that the set conditions did not cause element migration during apatite measurements. The analytical results have been corrected using the XPP on-line correction program (Pouchou and Pichoir, 1991). Natural and synthetic minerals and metals were used as standards and a detailed description of standards and detection limits can be found in the Supplementary material. The relative accuracy has been determined by measuring selected secondary standards as unknowns and is better than 3 % for major elements and better than 5 % for minor elements.

Element mapping was performed on the same instrument using 20 kV accelerating voltage, 100nA beam current, and a focused beam. Dwell time per pixel was set to 50 ms. The elements were assigned on the spectrometers to have only two sweeps per image with the beam sensitive elements F, Ca, K, and Na set to the first sweep. Images acquired were processed by software by supplied by John Donovan, using the mean atomic number (MAN) background correction method (Donovan and Tingle, 1996, Donovan et al., 2021). More information can be found in the supplementary information.

Table 1
Mineral assemblages and trace element contents of the representative samples.

Rock type	Do	Do	Do	B/M	B/M	B/M	B/M	S	S	S	V	V	V	The average detection limit
Name	BY153	BY35	BY28	BY111	BY136	BY06	BY25	BY260	BY52	BY226	Z13	19–1	12–2	
Mineral assemblages	D (dominated), M, Mz, B	D (dominated), M, F, R, Mz, Ap, B	D (dominated), M, Mz, B	R, P, M, Mz (Banded)	D, F, R, M, Ap, B (Banded)	A (Massive), Br, Ap, B, M	A, R, F, Br, Mz, B (Banded)	Bt, Q, C, Py	Bt, C, O, Ab, I, Py	Bt, O	A (dominated), C, Q	A (dominated), C, R, M, Ap	Coarse-grained A, REE fluorocarbonate, P, Mz, F, Ap, Br, M	
Sc	73	36	35	301	262	117	62	204	45	1.0	184	108	109	1
Nb	436	31	109	265	1250	1700	59	844	119	23	30	2930	758	1
La	9010	5680	1630	44,400	5120	6600	14,400	117	79	3.4	216	5750	15,200	3
Ce	18,000	10,150	5890	67,100	14,900	14,800	25,600	222	194	7.1	496	16,600	26,200	3
Pr	1935	1075	799	6080	2460	1665	2570	25	23	0.91	58	2010	2420	0.2
Nd	6150	3490	2620	19,150	11,000	5210	8070	102	110	4.9	201	7330	7460	0.5
Sm	434	284	148	1405	944	430	639	27	26	0.94	17	856	798	0.2
Eu	77	51	24	263	141	110	124	6.0	7.7	–	3.3	192	183	0.2
Gd	136	84	38.5	436	204	241	228	11.4	20	0.47	5.5	369	355	0.3
Tb	12.1	7.0	3.4	44	12.7	22	25	0.85	2.6	0.05	0.78	42	35	0.05
Dy	50	28	15	191	52	83	106	2.7	13	–	4.3	193	150	0.3
Ho	6.0	3.3	2.1	26	7.2	9.5	14	0.32	1.9	0.05	0.96	26	20	0.05
Er	10.0	6.1	4.1	42	15	15	23	0.53	3.8	–	2.9	49	36	0.2
Tm	0.83	0.58	0.42	3.2	1.6	1.2	1.8	0.05	0.40	–	0.43	3.8	2.9	0.05
Yb	4.0	2.7	2.0	13.6	9.0	4.1	7.5	0.25	2.1	–	3.1	13.4	11.3	0.2
Lu	0.38	0.28	0.24	0.99	1.03	0.34	0.72	0.05	0.26	–	0.47	1.15	1.13	0.05
Y	129	79	44	459	180	161	285	6.8	46	–	34	431	430	3
LREE	35,606	20,730	11,111	138,398	34,565	28,815	51,403	499	439.7	17.25	991.3	32,738	52,261	
HREE	348.31	210.96	109.76	1215.79	482.53	537.14	691.02	22.95	90.06	0.57	52.44	1128.35	1041.33	
Zr	10.0	20	10.0	30	10.0	40	60	591	295	10	22	20	90	10
Hf	1.00	1.00	1.00	3.0	1.00	1.00	2.0	37	9.2	–	4.5	2.0	6.0	1
Ta	0.50	0.50	0.50	0.50	0.50	0.50	0.50	1.1	0.50	–	–	–	0.50	0.5
Rb	2.0	5.0	1.00	29	1.00	1.00	2.0	120	125	211	2.6	1.00	23	1
Th	185	64	95	259	562	200	109	66	13	2.0	6.2	440	470	0.3
U	0.30	0.30	0.30	0.50	0.30	1.8	0.30	0.83	0.29	0.49	–	5.7	0.60	0.3
Sn	28	5.0	5.0	118	67	37	18	30	6.0	–	1135	568	99	5
W	5.0	5.0	5.0	5.0	5.0	5.0	5.0	7.0	3.0	–	–	–	–	5

Abbreviation of the rock type: Do: Ore-hosting dolomite; B/M: Banded/Massive ores; S: Slate/Schist; V: Vein type ores.
Abbreviation of the mineral:D: Dolomite; M: Magnetite; Mz: Monazite; B: Bastnäsite; F: Fluorite; R: Na-amphibole; Ap: Apatite; P: Phlogopite; A: Aegirine; Br: Barite; Bt: Biotite; Q: Quartz; C: Calcite; Py: Pyrite; O: Orthoclase; Ab: Albite; I: Ilmenite.
Trace element contents are displayed in ppm. '-' means below the detection limit.

3.5. LA-ICP-MS analysis

Trace element analyses were performed using a double-focusing single collector inductively coupled plasma mass spectrometer (ICP-MS) (AttoM, Nu Instruments Ltd., Wrexham, UK) coupled with an Excite 193 nm ArF excimer laser-ablation system (Photon Machines, San Diego, USA), at the Espoo Research Laboratory of GTK. Samples were ablated in a helium (He) atmosphere (0.4 to 0.1 l/min) within a HelEx II two-volume ablation cell, and the ablated aerosol was carried with a He-Ar gas mix (Ar flow = 0.85–0.95 l/min) towards the ICP. The gas mixture was optimized daily for maximum sensitivity. The laser was set to output 5 mJ energy at 2–5 % variation. The laser energy delivered on the samples was set between 30 % and 80 % for different minerals to achieve optimum ablation. By focusing on a 30 μm to 60 μm circular spot, the laser generated 2–8 J/cm^2 fluence. In general, ferromagnesian silicates, oxides, carbonates, phosphates, sulfides, and sulfates were ablated with a low fluence, whereas feldspars and fluorite were ablated with a higher fluence. The laser was run at a pulse frequency of 5 Hz for 200 shots. Each measurement was initiated with a 20-second baseline measurement followed by switching on the laser for 40 s for signal acquisition. Analyses were made using time resolved analysis (TRA) with continuous acquisition of data for each point (generally following the scheme of primary standard, quality control standards, 10–20 unknowns). The 1 sigma errors of each measurement are given in S upplementary Table S2 and S4. For all mineral phases but sulfides, USGS basaltic glass GSE-2 g was used as the primary standard; and BHVO-2 g, BCR-2 g, and NIST610 were used as quality controls for all but rutile and monazite, for which matrix-matched standards were used, i.e., R10 and TS-MNZ, respectively. For sulfides, pressed nano-pellets FeS1 was used as primary, FeS5 and FeS6 were used as quality controls.

Data reduction was performed with GLITTER4.4.4 software, and reference values for the standards were taken from GeoReM. Internal standards were a major element that had been measured by electron microprobe or EDS or using stoichiometric value if the former two analyses were not available.

3.6. Laser Raman analysis

Laser Raman spectrum was conducted using a HORIBA Jobin-Yvon LabRam HR 800 at the Institute of Geology and Geophysics, Chinese Academy of Sciences (IGGCAS). This system is equipped with a Peltier cooled multichannel CCD detector and coupled with an Olympus BX41 petrographic microscope. A frequency doubled Nd: YAG laser was used for excitation (λ = 532 nm, output laser power on the sample is 50mW) with a grating of 600 lines/mm, confocal hole set to 400 μm, and slit width set to 100 μm. Monocrystalline silicon with a Raman shift at 520.7 cm^{-1} was used as a calibration standard before measurement. The Raman spectra of the phases were acquired using a 100 × objective with an acquisition time of 30 s with three accumulations. The Raman spectral resolution achieved is < 1.0 cm^{-1}.

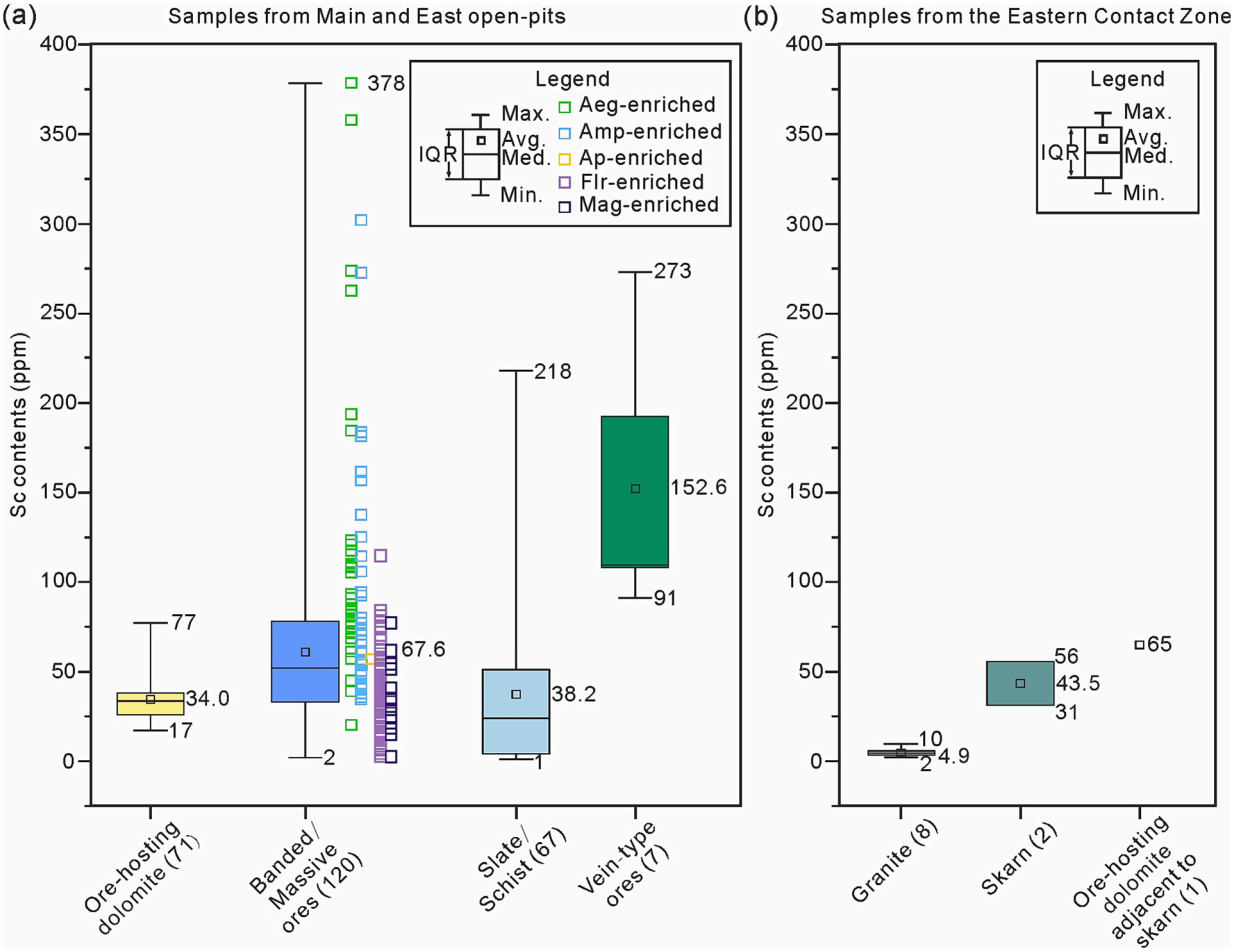

Fig. 4. Sc contents of different rock types in the Bayan Obo deposit, with the number of samples indicated in parentheses on the x-axis. (a) Samples from Main and East open pits. (b) Samples from the Eastern Contact Zone. Six data points for granite were taken from Yang et al., (2000). The Banded/Massive ores were further plotted (represented by squares) according to their mineral assemblage characteristics from Supplementary table 1.

4. Analytical results

4.1. Whole-rock Sc content

Bulk-rock Sc contents of the samples are provided in S upplementary Table S1, with sample locations shown in Fig. 3. At the deposit scale, the results show that the highest Sc contents (roughly > 100 ppm) are observed near the boundary between ore-hosting dolomite and the slate/schist. In contrast, Sc levels in the dolomite-dominated areas are consistently moderate to low, while both relatively high and minimal Sc values are found within the slate/schist-dominated areas.

At the individual hand sample scale, as illustrated by the box plot (Fig. 4a), the Sc contents of the ore-hosting dolomite range from 17 to 77 ppm (interquartile range (IQR) 26–38N = 71); banded/massive ores have 2–378 ppm (IQR 34–80, N = 120); the slates have 1–218 ppm (IQR 4–52, N = 67); the vein type samples have 91–273 ppm (IQR 108–193, N = 7).

In the profile sampled at the Eastern Contact Zone (Fig. 4b), the granitoids display low Sc whole-rock contents of 2–10 ppm (IQR 3.5–5.5, N = 8), consistent with the results of Yang et al. (2000). The skarn has Sc concentrations of 31 ppm and 56 ppm, which fall between the value of genetically related granitoids and ore-hosting dolomite.

4.2. AMICS quantitative and mineral classification maps

Thirteen samples with varying whole-rock Sc contents were selected to conduct thin-section modal weight composition mapping and geochemical analyses. Detailed descriptions including trace element concentrations are listed in Table 1. Mineral associations and texture as determined by the scanning μ-XRF mapping, and quantitative mineral proportions were computed with the AMICS software (Figs. 5, 6, 7, 8). The resulting mineral maps display only minerals with a mass percentage higher than 0.01 % in the sample.

The ore-hosting dolomites (BY153 with 73 ppm Sc, BY35 with 36 ppm Sc, and BY28 with 35 ppm Sc) are dominated by dolomite (>60 %) and disseminated or slightly oriented magnetite (>5%). Additionally, they contain subordinate and variable amounts of REE minerals, fluorite, and sodium/sodium-calcium amphibole (Fig. 5a, 5b).

The banded/massive ores (BY111 with 301 ppm Sc, BY136 with 262 ppm, BY06 with 117 ppm, and BY25 with 62 ppm) typically display intense metasomatism, and show variable mineral associations and directional textures (Fig. 6a, 6b). In sample BY111, the major minerals are Na-amphibole, monazite, biotite, and magnetite; BY 136, the major phases include fluorite, dolomite, Na-amphibole, and magnetite; BY 06 comprises primarily aegirine, magnetite, and barite; and BY 25, the major minerals are aegirine, Na-amphibole, fluorite, and barite.

Slate/schist samples (BY260 with 204 ppm Sc, BY52 with 45 ppm Sc, and BY226 with 1 ppm Sc) generally consist of biotite, calcite, quartz, and feldspar in different percentages and mineral textures (Fig. 7a, 7b). Both BY 260 and BY 52 are dominated by biotite with various accessory minerals, such as pyrite, fluorite, ilmenite, and apatite. In contrast, in sample BY 226, the major phase is feldspar, with disseminated or fracture-filling biotite. Notably, grains of jervisite were recorded in the Sc-rich sample BY 260.

Vein-type ores (Z13 with 184 ppm Sc, 19–1 with 108 ppm Sc, 12–2 with 109 ppm Sc) are characterized by dominant aegirine, with coarse-grained REE minerals, apatite, calcite, baryte, phlogopite, and fluorite heterogeneously deposited across different parts of the veins (Fig. 8a, 8b).

4.3. In-situ trace elements in minerals

Trace element compositions in the major mineral phases of each sample were determined by LA-ICP-MS (Supplementary Table S2). Fig. 9 illustrates a boxplot diagram showing Sc concentrations in major rock-forming minerals across different rock types. Amphibole and aegirine

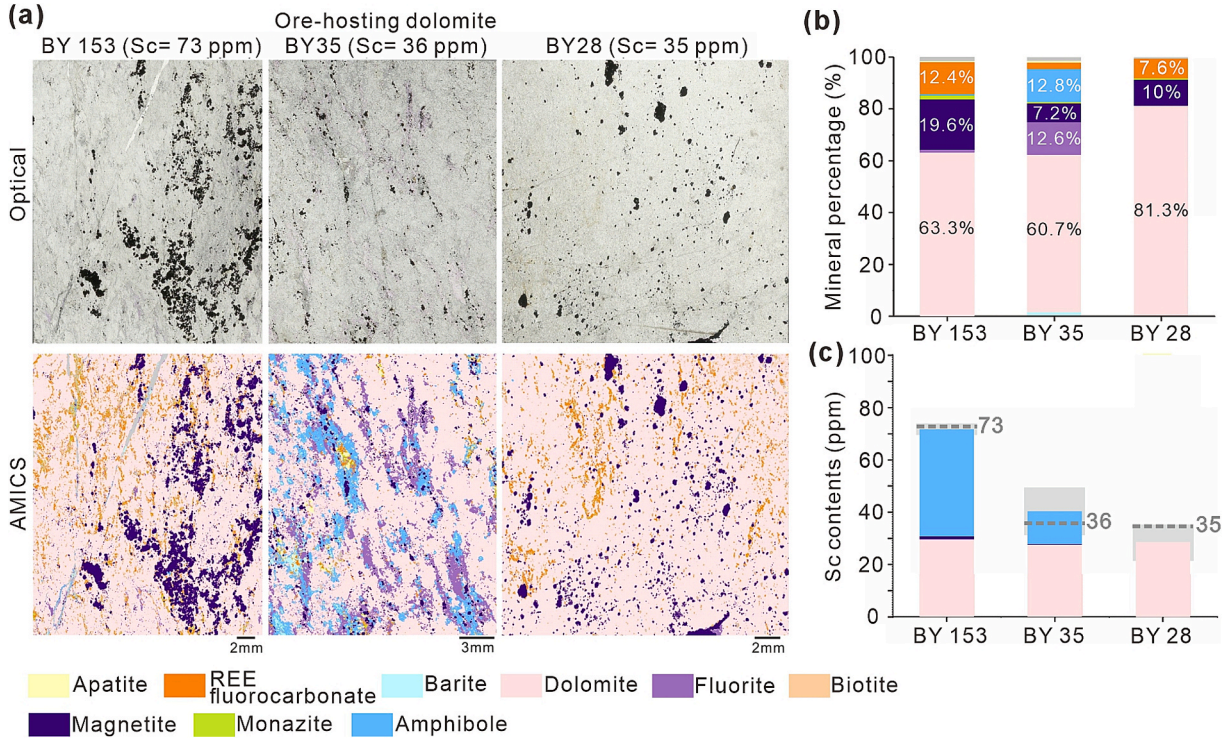

Fig. 5. Mineral assemblages and main Sc container of ore-hosting dolomite with different Sc contents. (a) The thin section maps and mineral assemblages of ore-hosting dolomite with different Sc contents. (b) The histogram of the mineral compositions of ore-hosting dolomite in Fig. 5a. (c) Contribution of Sc resources from different minerals of ore-hosting dolomite in Fig. 5a. The grey dash lines are the measured whole rock Sc contents of corresponding samples. The grey shadows represent the evaluated error of the recalculated whole rock Sc contents.

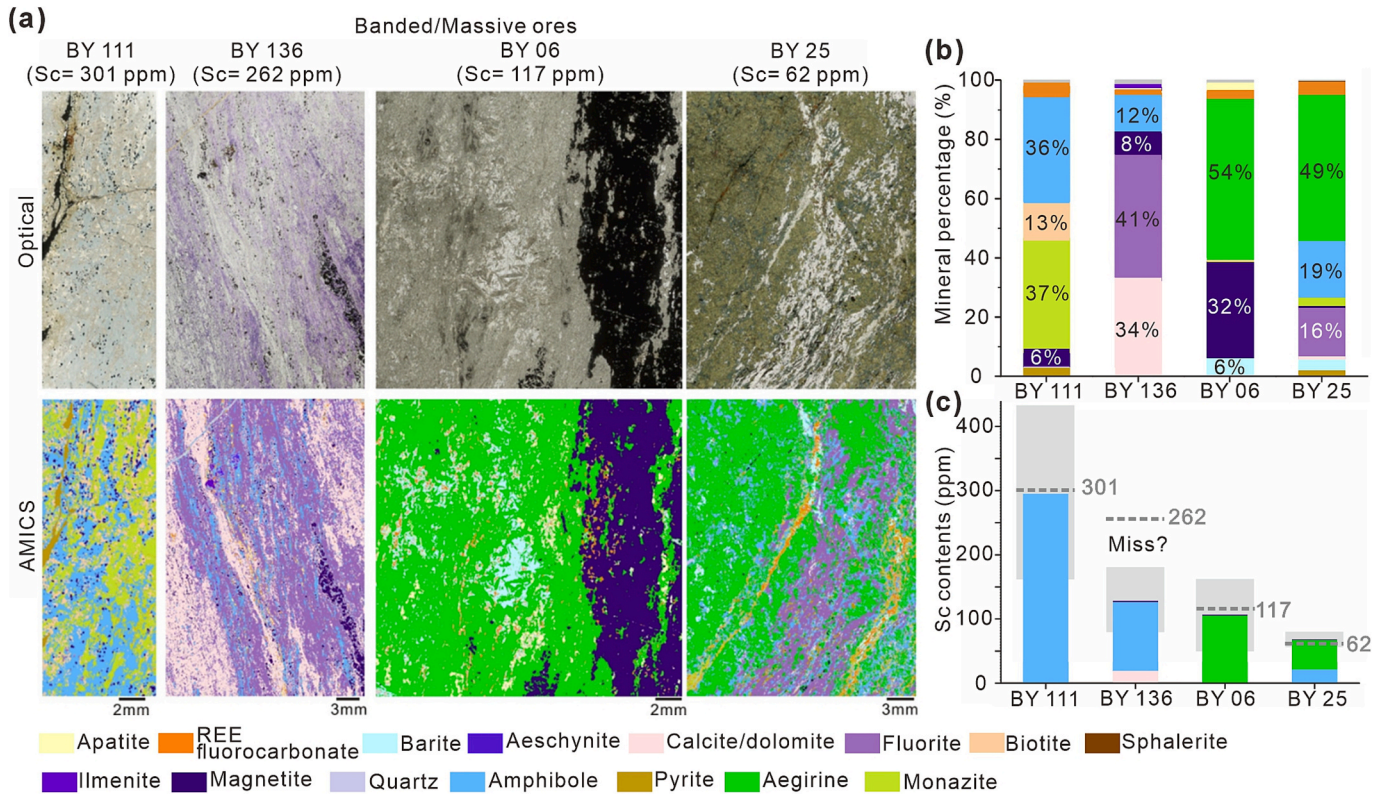

Fig. 6. Mineral assemblages and main Sc container of banded/massive type ores with different Sc contents. (a) The thin section maps and mineral assemblages of banded/massive type ores with different Sc contents. (b) The histogram of the mineral compositions of banded/massive type ores in Fig. 6a. (c) Contribution of Sc resources from different minerals of banded/massive type ores in Fig. 6a. The grey dash lines are the measured whole rock Sc contents of corresponding samples. The grey shadows represent the evaluated error of the recalculated whole rock Sc contents.

in all rock types as well as mica and ilmenite in slate/schist consistently exhibit elevated Sc (over 50–100 ppm). Notably, aegirines in vein-type ores display relatively higher and variable Sc concentrations (46–956 ppm, averaging ca. 342 ppm) compared to those in the banded/massive ores (67–501 ppm, averaging ca. 157 ppm). Dolomite has uniform Sc concentrations/contents (ca. 46 ppm), lower than amphibole and aegirine, but significantly higher than calcite (ca. 7 ppm). In contrast, magnetite, calcite, monazite, apatite, feldspar, fluorite, and barite consistently display low Sc contents in all rock types.

Moreover, to determine whether in-situ analysis overlooked any Sc-rich minerals, overall Sc contents were calculated by considering mineral proportion and their corresponding Sc content using the following equation, which was then compared with the XRF and ICP-MS bulk results (Fig. 5c, 6c, 7c, 8c):

$$C_{recalculated-Sc} = \sum (C_{i.ave} \times P_i) \pm error \quad (1)$$

where $C_{recalculated-Sc}$ is the recalculated whole-rock Sc content, $C_{i.ave}$ is the average Sc contents of mineral i, and the P_i is the mineral proportion of i in the corresponding sample (given by AMICS analysis, Supplementary Table S3). The error adhered to the eq. (1) was calculated based on a random error propagation equation (Zou, 2014) as follows:

$$error = \sqrt{\sum (P_i^2 \sigma_i^2)} \quad (2)$$

in which the σ_i is the standard deviations of $C_{i.ave}$

In the ore-hosting dolomite, the $C_{recalculated-Sc}$ closely corresponds to the measurements (Fig. 5c). Dolomite exhibited relatively uniform Sc (41.9 ± 11.6 ppm, 1σ), whereas amphibole had a significant variability in Sc (from 1 wt% to several tens of ppm) contents. The Sc content of amphibole is much higher in BY-153 than BY-35, despite having much lower amphibole contents. It implies that the Sc content of the amphibole may be more important in determining whole rock values than the amount of amphibole. However, more data is required to make such a conclusion robust.

In the banded/massive ores (Fig. 6c), the calculated overall Sc concentrations of samples BY111, BY06, and BY25 matched the bulk-rock measurements, unveiling significant contributions from aegirine and amphibole. However, the wide uncertainty ranges in the calculation value imply the heterogeneity of the Sc content within these two major Sc contributors in this rock type. In contrast, the calculated Sc concentrations of the sample BY136 are notably lower than the measured values, persisting even after considering the uncertainty. This Sc deficit implies the missing of some specific Sc-enriched phases in the calculation.

In the slate (Fig. 7c), the calculated overall Sc contents closely matched the bulk measurements. Among the predominant rock-forming minerals, biotite emerges as the primary source of Sc, while feldspar seems to have a negligible contribution. The varying proportions of mica and its Sc concentration likely account for the variations in whole-rock Sc contents. In high-Sc slates, jervisite emerges as a significant contributor, despite its small proportion in the rock.

In vein-type ores (Fig. 8c), aegirine stands out as the primary source of the Sc. Notably, the calculated overall Sc contents exhibit the widest uncertainty range, generally surpassing the measurements or aligning with the lower boundary of uncertainty with 1σ error such as in samples Z13 and 12–2. This underscores the substantial heterogeneity inherent in vein-type rocks. On the one hand, Sc contents of aegirine display non-uniformity; on the other, these rocks exhibit variable mineral associations (Fig. 2d; Fig. 8b). The latter usually overestimates the aegirine content and further leads to a higher whole-rock Sc-calculated value compared to the measured ones (Fig. 8c).

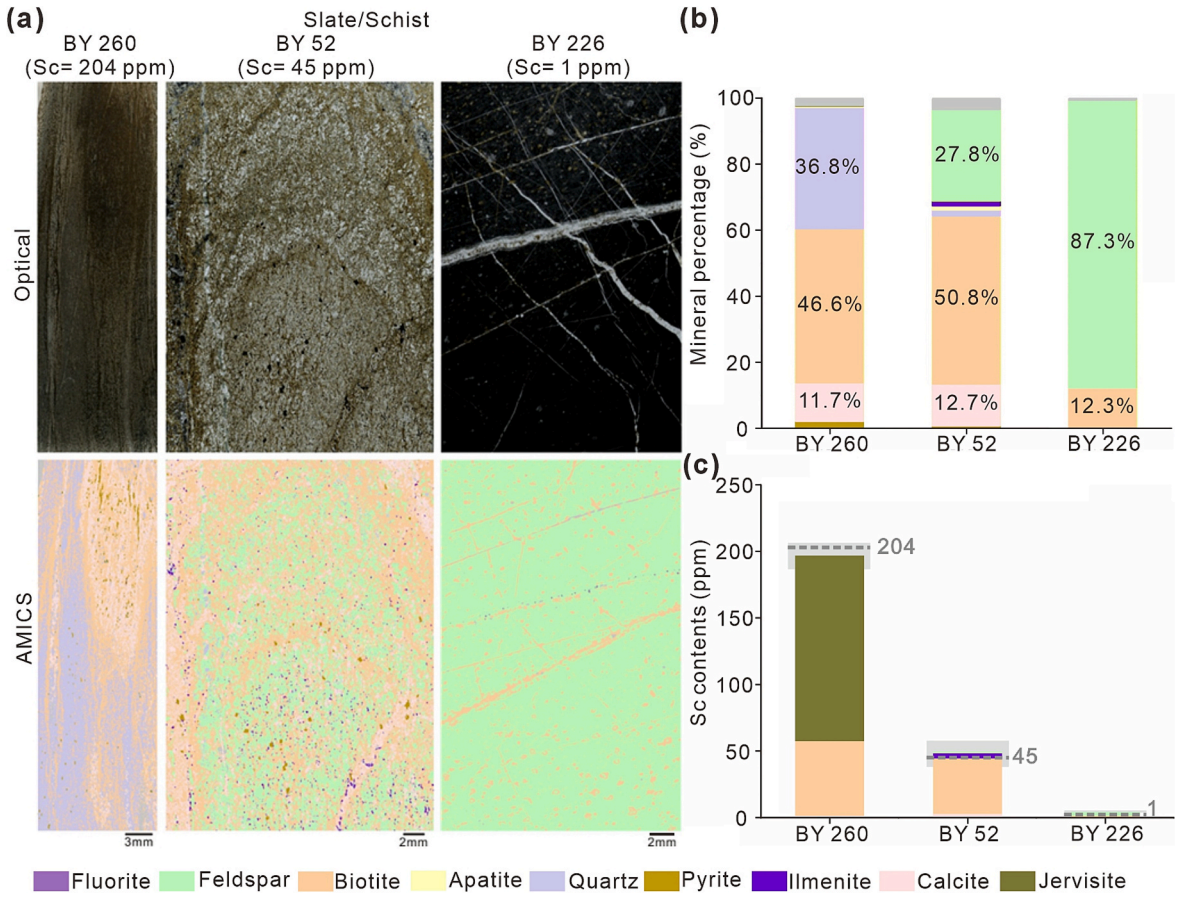

Fig. 7. Mineral assemblages and main Sc container of slate/schist with different Sc contents. (a) The thin section maps and mineral assemblages of slate/schist with different Sc contents. (b) The histogram of the mineral compositions of slate/schist in Fig. 7a. (c) Contribution of Sc resources from different minerals of slate/schist in Fig. 7a. The grey dash lines are the measured whole rock Sc contents of corresponding samples. The grey shadows represent the evaluated error of the recalculated whole rock Sc contents.

4.4. Chemical composition and microtexture in Sc-mineral

In addition to mineral associations, μ-XRF mapping delineates the distribution of Sc concentrations at thin section scales. The distribution maps reveal heterogeneously scattered Sc hot-spots (>~0.3 wt% Sc) in pixel sizes with a volume percentage lower than 0.1 ‰ (Fig. 10). The compositions and microstructure of these hot spots are further studied by BSE, EPMA, LA-ICP-MS, and laser Raman, and three distinct types of Sc minerals are identified (Fig. 11; Tables 2, 3, 4).

The first Sc-rich mineral is thortveitite, containing the Sc concentration of 48–54 wt% and is found in the banded/massive ores (Table 2, Fig. 12a). The second Sc-mineral is a solid solution series of pyroxene with two end members, ideal aegirine and jervisite. The Sc-bearing aegirine occurs in both banded/massive ores and vein-type ore, with the Sc_2O_3 contents of 0–7 wt%, while jervisite was found only in the slate, with the Sc_2O_3 contents of ca. 24 wt% (Table 3, Fig. 12c, 12d). A third Sc-rich mineral occurs in the banded/massive ores and is a hydrous silicate mineral, exhibiting a high concentration of Be, and Sc_2O_3 contents of 13–14 wt% (Table 4, Fig. 12e, 13; Supplementary Table S4). It thus should be bazzite, according to the major composition calculation. However, due to particle size and quantity limitations, only the trace element components of aegirine-jervisite and bazzite could be measured (S upplementary Table S4).

Quantitative EPMA elemental mapping was performed on four grains representing each of the three types of Sc-mineral. The Sc concentration distribution maps for these grains are presented in Fig. 12, while maps for other elements can be found in the S upplementary Figures. The Sc distribution shows zoning textures with sharp and irregular compositional boundaries in the Sc-bearing aegirine (Fig. 12g). The concentration in the core region is up to 3–7 wt%, significantly higher than in the rim regions. The Sc content in jervisite was relatively uniform across the mineral, with only a limited area near fractures showing a gradually decreasing trend in Sc concentration (Fig. 12h). The other two types of Sc mineral demonstrate a relatively homogeneous composition and closely coexist with Sc-bearing amphibole (Fig. 12f, 12i).

5. Discussion

5.1. Main Sc-carrying mineral

Clarifying Sc speciation is crucial for understanding the Sc enrichment processes within an ore deposit. In the Bayan Obo carbonatite system, our detailed investigation, conducted from the mine- to mineral grain-scale, systematically reveals the main Sc-carrying minerals and the significant enrichment in forming individual Sc phases as follows:

(1) In common rock-forming minerals, aegirine and Na-amphibole typically exhibit the highest scandium (Sc) concentrations across all rock types, whilst biotite and ilmenite are the primary Sc carriers in slate and schist. The whole-rock Sc budget is influenced by both the abundance of these minerals and their Sc content. Notably, the Sc concentration in amphibole is significantly higher in sample BY-153 than in BY-35, resulting in a higher whole-rock Sc content in BY-153, even though it contains less amphibole overall. It suggests that Sc content in amphibole may play a more critical role in determining whole-rock Sc levels than mineral abundance alone, while additional data are needed to further validate this observation. In contrast, magnetite, fluorite, apatite,

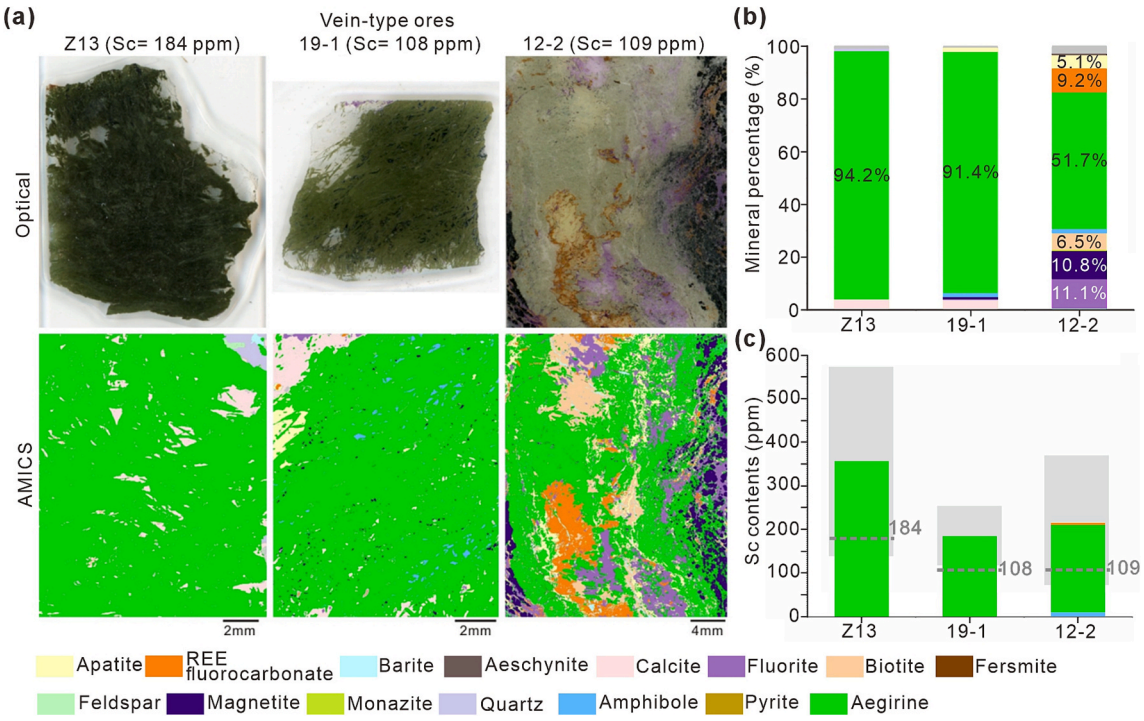

Fig. 8. Mineral assemblages and main Sc container of vein-type ores with different Sc contents. (a) The thin section maps and mineral assemblages of slate/schist with different Sc contents. (b) The histogram of the mineral compositions of vein-type ores in Fig. 8a. (c) Contribution of Sc resources from different minerals of vein-type ores in Fig. 8a. The grey dash lines are the measured whole rock Sc contents of corresponding samples. The grey shadows represent the evaluated error of the recalculated whole rock Sc contents.

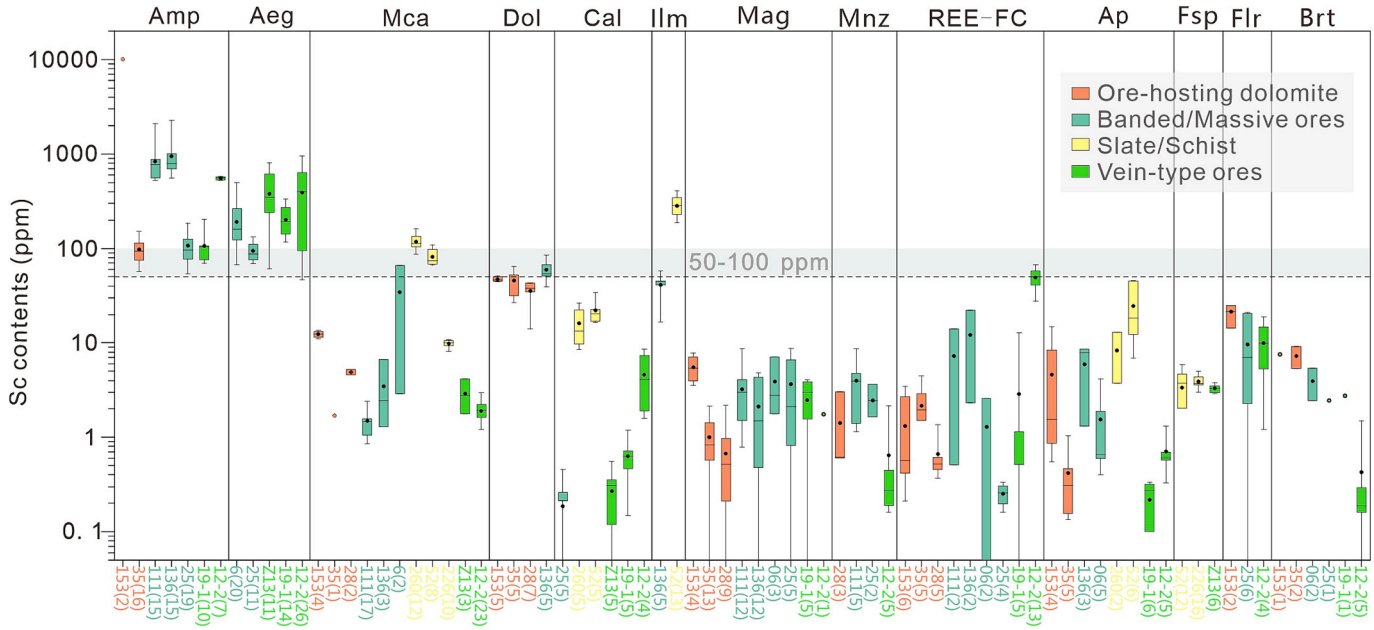

Fig. 9. Sc contents of different minerals in different types of rocks, with the number of data indicated in parentheses on the bottom x-axis. The abbreviation of the mineral type is marked at the top x coordinate. The y-axis is on a logarithmic scale. Color represents the different rock types. Amp: amphibole, Aeg: aegirine; Amp: amphibole; Ap: apatite; Brt: barite; Cal: calcite; Dol: dolomite, Flr: fluorite; Fsp: feldspar; Ilm: ilmenite; Mag: magnesite; Mca: mica; Mnz: monazite; REE-FC: fluorocarbonates of rare earth elements minerals.

feldspar, barite, and REE-fluorocarbonate have very low concentrations of Sc (Fig. 9). Additionally, some columbite is found to contain 1–2 wt% of Sc_2O_3 as mineral inclusion in magnetite or mafic minerals, i.e. biotite, with a very small mineral abundance (Supplementary material; Shimazaki et al., 2008, Yang et al., 2022).

These Sc occurrences at Bayan Obo support the substitution of Fe, Mg, and Ti-Nb-Ta by Sc, facilitated by a similar charge density in the crystal (Samon and Chassé, 2016; Siegfried et al., 2018). It indicates that Sc extraction from ferromagnesian silicates and Ti-/Nb-bearing minerals could be important for the efficient extraction of Sc resources in the Bayan Obo deposit. Numerous roasting experiments have confirmed the acid-leaching process for Sc from amphibole and aegirine (Zhang et al.,

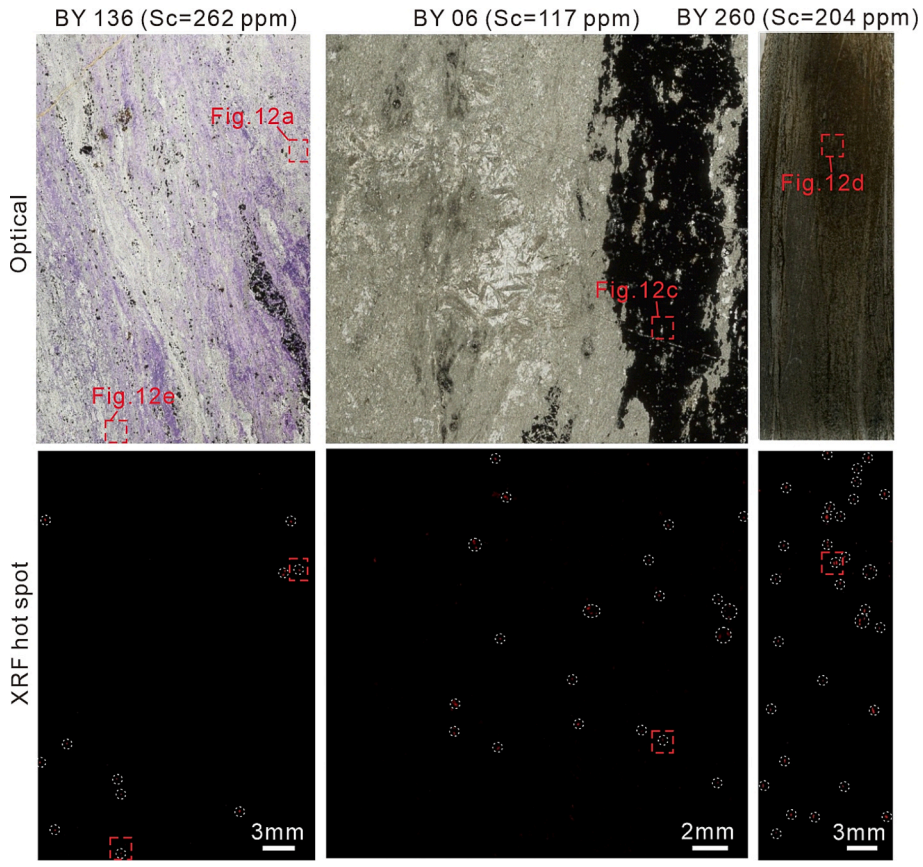

Fig. 10. The Sc hot-spot distribution in thin section scale based on the μ-XRF mapping. The whole-rock Sc contents of the samples are marked on the top. Red dots are Sc hot spots also marked with dashed white circles. The BSE ma images of the Sc hot spot in the dashed red squares are given in Fig. 12.

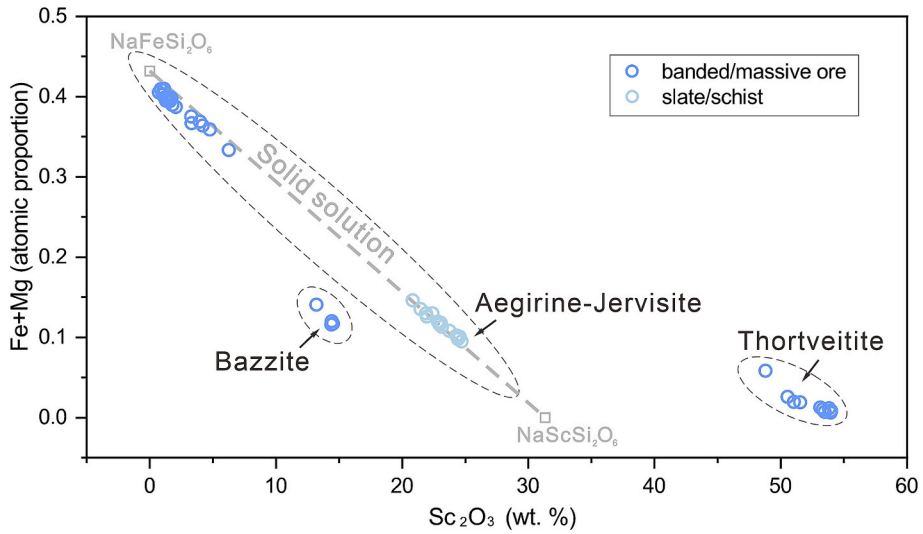

Fig. 11. Different types of individual Sc minerals, distinguished by the diagram of Sc_2O_3 vs. (Fe + Mg) atomic proportion, based on Electron Microprobe analysis. Colors represent the rock types.

2019; Bao et al., 2022; Shao et al., 2023). It is necessary to develop a ferromagnesian silicate-oriented beneficiation process with high separation efficiency for Sc, as it is an unavoidable Sc extraction process but significant environmental impacts (Wang et al., 2020). However, it is still difficult to obtain high-grade Sc concentrates through mineral processing to improve its separation efficiency. Acid leaching of silicates in tailings/waste of Nb and Fe processes might be a cost-effective alternative, considering the development potential of Nb.

(2) In recent years, individual Sc minerals have been frequently discovered, mainly in pegmatites, such as Iveland-Evje, Tørdal, Jordanów Śląski (Kolitsch et al., 2010; Stokkeland, 2016; Pieczka et al., 2024a, 2024b, 2024c). However, so far only thortveitite ($Sc_2Si_2O_7$) and supergene mineral juonniite ($CaMgSc[PO_4]_2{\cdot}4H_2O$) have been reported in carbonatite-related systems (Amli, 1977; Kalashnikov et al., 2016). This study is the first to identify three types of individual Sc silicate minerals in the Bayan Obo carbonatite system, in samples with whole-

Table 2
The major element concentrations of representative thortveitite given by electron micro-probe analysis in wt. %.

Sample Name	136_1-1	136_5-3	136_6-3
F	0.00	0.00	0.00
CaO	0.33	0.68	0.23
Sc_2O_3	53.95	53.47	53.32
P_2O_5	0.00	0.00	0.00
FeO	0.37	0.48	0.66
MnO	0.04	0.11	0.03
TiO_2	0.00	0.00	0.00
K_2O	0.01	0.01	0.01
Nb_2O_5	0.01	0.01	0.00
Na_2O	0.00	0.01	0.01
SiO_2	45.55	46.06	45.80
MgO	0.03	0.02	0.04
Al_2O_3	0.07	0.08	0.05
Total	100.36	100.93	100.15

rock Sc contents of > 100 ppm, namely: aegirine ($NaFe^{3+}Si_2O_6$) – jervisite ($NaScSi_2O_6$) solid solutions, bazzite ($Be_3Sc_2Si_6O_{18}$), and thortveitite ($Sc_2Si_2O_7$).

Identifying these minerals in the deposit is still challenging due to their extremely small abundance (<0.1 ‰) and fine grain size. They are therefore also challenging to identify under the optical microscope, thus micron-scale XRF scanning with sufficient resolution (around 20 μm) becomes a nearly indispensable method. However, setting small step sizes can significantly increase the analytical time. Therefore, understanding the control factor of Sc distribution and identifying genuinely promising samples and regions are crucial for locating independent Sc minerals (see the sections below). Although they are unlikely to become economically viable for specialized mining and recovery, the discovery of multiple types of individual Sc-minerals confirms the extreme enrichment of Sc in carbonatite systems and the potential for finding new Sc-minerals in the Bayan Obo deposit.

Furthermore, the comparison of Sc distribution in other Sc-rich carbonatites with the Bayan Obo deposit indicates that Sc occurs in various phases in these carbonatite systems also. For example, in the Elk Creek deposit (USA), carbonates account for 68.5 % of the total Sc (1,644 t; Verbaan et al., 2018). The Kovdor deposit (Russia) features Sc-bearing baddeleyite (Kalashnikov et al., 2016), while bulk-rock Sc contents at Tomtor (Russia) range from approximately 100–750 ppm (Lapin et al., 2016). In the Fen deposit (Norway), Sc is reported in thortveitite (Amli, 1977). These occurrences appear at first sight to be inconsistent with Bayan Obo, where Sc is typically associated with mafic minerals and HFSE-rich minerals corresponding with Sc geochemistry. However, significant fenitization and Nb reserves have also been reported in these systems, such as Fen, Elk Creek, and Tomtor. Systematic sampling and comprehensive mineral analyses of Sc-rich fenites and HFSE-rich minerals (e.g., Nb speciation) in these deposits may therefore expand the knowledge of Sc speciation in these complex carbonatite systems. An alternative explanation for this discrepancy is the difference in ore-forming environment. Our study does not have adequate information to resolve these issues but we provide some preliminary insight below.

5.2. Key control on Sc distribution

The emplacement of carbonatite melts into the crust can be accompanied by *syn*-magmatic fluids, which may cause metasomatism of the country rocks (Yaxley et al., 2022). These two processes, magma crystallization and metasomatism by expelled hydrothermal fluids, differently control the distribution of economic resources in the deposit, with Fe mineralization primarily associated with the former and REE distribution driven by the latter (Anenburg et al., 2021; Chen et al., 2024). While Sc has a much smaller ionic radius than other REEs and exhibits characteristics of a more compatible element (Shannon, 1976, Williams-Jones and Vasyukova, 2018), our findings at deposit- to crystal- scales indicate that, like other lanthanides, its distribution in the Bayan Obo carbonatite deposit is primarily controlled by hydrothermal alteration.

At the deposit-scale, rocks with high Sc concentrations commonly occur in the strongest alkaline alteration zones, located in the vicinity of the contact zone between the H9 slate/schist and the ore-hosting dolomite (Fig. 3; Yang et al., 2023b). It is consistent with the observation that banded/massive and vein-type ores formed by alkaline alterations display higher Sc contents (2–378 ppm) compared to their protolith-dolomitic carbonatite and slate/schist (Fig. 4; Liu et al., 2018; Tang et al., 2021; Wei et al., 2022; Li et al., 2024). Despite the dolomitic carbonatite and slate/schist generally retaining their original magmatic

Table 3
The major elements concentrations of representative aegirine-jervisite solid solution given by electron micro-probe analysis.

Sample Name	06-15_1	06-17_5	06-27_2	06-18_5	06-24_2	260_30-1	260_4-2	260_6-2
CaO (wt. %)	0.84	0.30	0.12	0.16	0.18	3.91	1.86	2.86
Sc_2O_3	0.26	2.94	1.20	4.43	0.88	21.95	24.47	23.04
Fe_2O_3	33.79	30.98	33.08	29.48	33.17	8.52	7.27	8.22
MnO	0.03	0.01	0.00	0.01	0.03	0.16	0.09	0.13
TiO_2	0.04	0.00	0.00	0.00	0.00	0.00	0.00	0.00
K_2O	0.01	0.00	0.00	0.01	0.01	0.02	0.06	0.04
Na_2O	13.67	14.12	14.16	14.07	14.15	12.00	13.00	12.26
SiO_2	52.82	53.19	53.10	53.60	53.13	53.14	53.62	53.62
MgO	0.34	0.10	0.03	0.05	0.04	0.77	0.33	0.60
Al_2O_3	0.40	0.87	0.88	1.00	0.88	0.24	0.12	0.14
Total	98.83	99.44	99.28	99.86	99.18	99.86	100.09	100.10
T (ideally 2 apfu.)								
Si	1.98	1.97	1.97	1.98	1.98	1.97	1.98	1.99
Al	0.02	0.03	0.03	0.02	0.02	0.01	0.01	0.01
Fe^{3+}	0.01	0.00	0.00	0.00	0.00	0.02	0.02	0.01
T total	2.00	2.00	2.00	2.00	2.00	2.00	2.00	2.00
M1 (ideally 1 apfu.)								
Al	0.00	0.01	0.01	0.02	0.01	0.00	0.00	0.00
Fe^{3+}	0.94	0.86	0.92	0.82	0.93	0.22	0.19	0.22
Sc	0.01	0.09	0.04	0.14	0.03	0.71	0.79	0.74
Mg	0.02	0.01	0.00	0.00	0.00	0.04	0.02	0.03
M1 total	0.97	0.97	0.98	0.99	0.97	0.98	0.99	1.00
M2 (ideally 1 apfu.)								
Ca	0.03	0.01	0.00	0.01	0.01	0.16	0.07	0.11
Na	0.99	1.01	1.02	1.01	1.02	0.86	0.93	0.88
M2 total	1.03	1.03	1.02	1.01	1.03	1.02	1.01	1.00

Table 4
The major elements concentrations of bazzite given by electron micro-probe analysis.

Sample name	136_10-1	136_10-2	136_10-3	136_14-1
SiO_2 (wt. %)	59.64	59.41	59.71	60.09
Al_2O_3	0.20	0.18	0.22	0.36
Fe_2O_3	4.68	5.57	4.68	6.08
MnO	0.31	0.39	0.33	0.28
MgO	2.35	1.87	2.47	2.59
CaO	0.62	0.36	0.30	0.09
Na_2O	2.72	2.72	2.67	2.42
K_2O	0.19	0.20	0.21	0.21
*BeO	12.41	12.37	12.43	12.51
Sc_2O_3	14.51	14.38	14.40	13.21
*Total	97.63	97.45	97.42	97.83
*H_2O	2.37	2.55	2.58	2.16
Formula proportions normalized to 6Si atoms				
T (apfu.)				
Si	6	6	6	6
X (apfu.)				
Al	0.02	0.02	0.03	0.04
Fe	0.35	0.42	0.35	0.47
Mn	0.03	0.03	0.03	0.02
Mg	0.35	0.28	0.37	0.39
Sc	1.27	1.27	1.26	1.15
Total X	2.03	2.03	2.04	2.06
A (apfu.)				
Be	3	3	3	3
R (apfu.)				
Ca	0.07	0.04	0.03	0.01
Na	0.53	0.53	0.52	0.47
K	0.02	0.03	0.03	0.03
Total R	0.62	0.58	0.58	0.50
Total Cation	11.03	11.03	11.04	11.06

"*" is a calculated assuming Be/Si = 0.5 and Total of 100 %.

or metamorphic characteristics, some of them are affected by hydrothermal alteration (Fig. 2f, 2g), and display a wide range of Sc contents, particularly for the slate/schist (1–218 ppm). If one considers the petrography, the high-Sc altered slate primarily comprises euhedral/subhedral biotite, coarse-grained calcite, albite, and orthoclase, along with some disseminated accessories such as pyrite, titanite, zircon, and jervisite (Fig. 2g, 7; Supplementary material), which are products of hydrothermal alteration (Li et al., 2022). In contrast, the Sc-poor slate/schist is characterized by metamorphic micrite feldspar and disseminated anhedral biotite, typical of fresh slate (Fig. 2h, 7; Supplementary material). Likewise, in the ore-hosting dolomite, the variation of Sc contents is predominantly controlled by Na-amphibole which is formed by the hydrothermal alteration (Fig. 5c; Liu et al., 2018).

At the rock- and mineral-scale, hydrothermal alteration creates distinct mineral assemblages within the banded and massive ores (Fig. 6a; She et al., 2021). Sc tends to concentrate in aegirine and amphibole but is absent in minerals like fluorite, and apatite, although all of these minerals are formed by hydrothermal alteration (Fig. 9). This mineralogical heterogeneity explains the substantial variation in Sc content within these ores. For example, massive ores rich in fluorite or magnetite typically show low Sc concentrations, while those with a high proportion of amphibole or aegirine—such as silicate-dominated banded ores and vein-type ores—are more promising as potential Sc resources (Fig. 4a). Besides, in addition to common rock-forming minerals, all observed individual Sc-minerals show evidence of hydrothermal metasomatism, indicated by their structural associations with surrounding minerals (Fig. 12).

In contrast, while the magmatic dolomite in this deposit shows relatively higher Sc contents than typical carbonatite (Wang et al., 2021), the levels are not significantly greater than those in most ultramafic or mafic rocks which generally lack substantial economic value

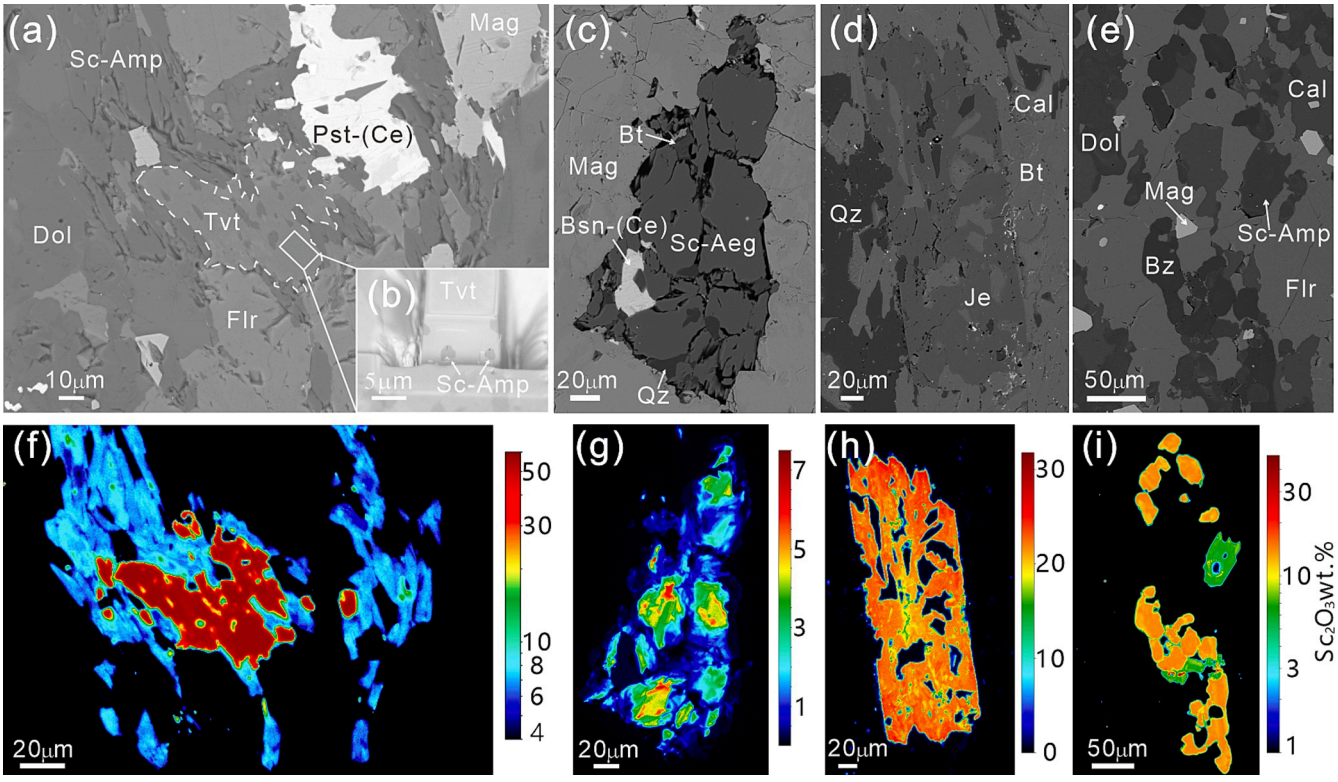

Fig. 12. The BSE images and EPMA mapping of Sc contents of individual Sc minerals in Fig. 11. The locations of the grains are given in Fig. 10. (a) thortveitite (BY136_1). (b) the thortveitite grain cut by FIB showing the amphibole inclusion. It shows the amphibole inclusion in thortveitite. (c) Sc bearing aegirine (BY06_18). (d) jervisite (BY260_33). (e) bazzite (BY136_10). (f-i) are the EPMA quantified maps of (a, c, d, e) showing Sc_2O_3 concentrations, with maps (f and i) in log scale. Sc-Amp: Sc-bearing amphibole; Dol: dolomite; Tvt: thortveitite; Flr: fluorite; Pst-(Ce): Parisite-(Ce); Mag: magnetite; Bt: biotite; Bsn-(Ce): bastnäsite; Sc-Aeg: Sc-aegirine; Qz: quartz; Cal: calcite; Je: jervisite; Bz: bazzite.

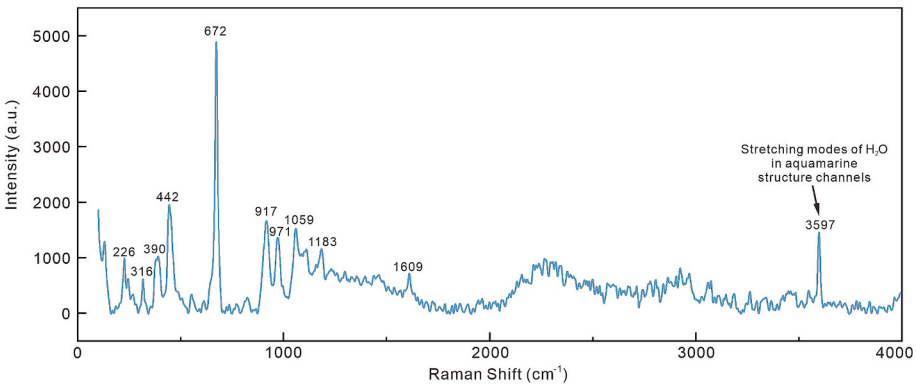

Fig. 13. The Raman spectral of the bazzite with a strong raman peak at 3597 cm-1. The position of the strong band represents the stretching modes of H_2O in aquamarine structure channels (Hagemann et al., 1990).

(Wang et al., 2021). Based on observations across different scales, we therefore suggest that Sc enrichment from subsequent hydrothermal fluids is more influential in Sc distribution than its magmatic origins. Fluid alteration has also been suggested as an important factor contributing to resource enrichment in the Elk Creek and Fen carbonatites (Dietzel et al., 2019; Verplanck et al., 2022;), although their Sc distribution patterns differ from the Bayan Obo, as mentioned before. One possible explanation for this difference is the variation in fluid composition. For instance, Elk Creek significantly lacks fluorine compared with Bayan Obo, while F-rich fluids can promote Sc migration into fenitizaiton zones rather than retention in carbonates (Wang et al., 2022a). Additionally, the properties of the surrounding rocks, such as permeability, may influence Sc distribution. In Bayan Obo, the slate/schist/sandstone of country rocks offer higher permeability compared with the granitic-gneisses in Elk Creek and Fen, facilitating alkaline F-rich fluid to migrate and form extensive fenitization supporting Sc precipitation therein.

5.3. The remobilization of Sc mineralization and implication

The diverse forms of Sc occurrences and detailed petrography reveals a multi-stage mineralization process for Sc in the Bayan Obo deposit. Sc-bearing Na-amphibole was altered and rimed/coated by thortveitite (Fig. 12a, 12b), a typical reaction texture indicating the former's earlier formation compared to the latter. Moreover, aegirine exhibits metasomatic textures characterized by a high-Sc core of 3–7 wt% and a metasomatized Sc-depleted rim around hundreds of ppm (Fig. 12c, 12g). Similar reaction zonings of Sc have also been observed in fluid-affected garnet and epidote-group minerals (Ismail et al., 2014; Čopjaková et al., 2015; Steffenssen et al., 2020; Pieczka et al., 2024a), differing from kinetic-induced texture in magmatic diopside (Wang et al., 2022b). These microtextures point to at least two significant Sc migrations and precipitation in the Bayan Obo deposit, with an earlier stage Sc precipitates in ferromagnesian silicates combined with alkaline alterations. At a later stage, Sc is remobilized and forms individual Sc-minerals with increased Sc enrichment, such as thortveitite.

It is also noteworthy that the observed reaction and metasomatic textures are not only exclusive to Sc minerals but also occur in monazite, bastnasite, zircon, and Nb-minerals of this deposit (Li et al., 2021a, 2021b; Zhan et al., 2023; Wang et al., 2024). The Sm-Nd, Th-Pb, and U-Pb isotopes support the interpretation that these minerals experienced fluid-aided modification, without significant outside lanthanides input, in which Nb and REEs experience multiple precipitation and remobilization (at ca. 1.3 Ga, 440 Ma and/or 270 Ma; Smith et al., 2015; Li et al., 2021b; Ren et al., 2023; Yu et al., 2024; Zhu et al., 2024) with abundant nuclidic signatures inherited from 1.3 billion years ago being partially or completely redeployed. The similar core-rim texture of Sc and other REEs implies the redistribution of Sc resources by subsequent fluid-associated events. These later alteration fluids have been categorized into H_2O-CO_2-NaCl-(F-REE) system with a high grade of fluorine (Fan et al., 2006; Li et al., 2023; She et al., 2023), and these components, especially F and OH, are proven to contribute significantly to the dissolution and migration of Sc by solubility experiment (Wang et al., 2022a, 2023), which corresponds to the highest average Sc value of vein type ore among other rocks types (Fig. 4). This suggests that both the ca. 440 Ma and ca. 270 Ma fluoride-enriched geological events had equal chance to play a role in remobilizing Sc and forming the metasomatism texture of Sc-bearing minerals that we see today. Therefore, geochronological studies of Sc-bearing mineral textures could be of interest in determining whether Sc experienced similar remobilization processes with lanthanides, and in elucidating the relationship between Sc and later significant alteration events, thereby aiding further exploration of Sc.

6. Conclusion

Observations at different scales have revealed the extreme enrichment of Sc resources in the Bayan Obo carbonatite system. The Sc resources in this deposit are commonly contained within aegirine, Na-amphibole, as well as biotite and titanite, which frequently occur in the banded/massive type ores, vein-type ores, and altered slate/schist. Three individual Sc minerals (thortveitite, aegirine-jervisite solid solutions, and bazzite) are identified for the first time at Bayan Obo, with a volume ratio of less than 0.1 ‰.

A hydrothermal process emerges as the main controlling factor of Sc enrichment. Samples exhibiting intense hydrothermal alteration are more likely to display elevated whole-rock Sc contents, especially in the vicinity of the contact zone between the H9 slate/schist and the ore-hosting dolomite.

The Sc concentration, texture, and assemblages of the different Sc-bearing species implies at least two significant Sc migration and precipitation events in the geological history of the Bayan Obo deposit. It is speculated that Sc is partially enriched through later hydrothermal processes into individual Sc minerals from ferromagnesian silicates.

Declaration of competing interest

The authors declare that they have no known competing financial interests or personal relationships that could have appeared to influence the work reported in this paper.

Acknowledgments

We appreciate helpful discussions with Lehtonen Marja, Hongping He, Xiaoyong Yang, Xiaochun Li, Hugh O'Brien, Quentin Dehaine, Matti Kurhila, Mia Tiljander, Minna Myllyperkiö, Tegist Chernet, Jukka Kuva,

Krisztian Szentpeteri, Jing Xu, Xiangping Gu, Tao Wang, Ting Li, and Jian Zhao. We also appreciate constructed comments from David Cooke, Iain Samson, and Anthony E. Williams-Jones. We are grateful to two anonymous referees for their constructive feedback that helped to improve the manuscript. This study was supported by the National Natural Science Foundation of China (42402094, 41930430), the Research Council of Finland (formerly Academy of Finland) via the Raw Materials Research Infrastructure (RAMI) Projects 337560 and 319602, the National Key R&D Program of China (grant 2021YFC2901704), the Traceability of Primary Mineral Resources and Recovery and Recycling of Secondary Mineral Resources Project (P22017) and the Key Research Program of the Institute of Geology and Geophysics, CAS (IGGCAS-201901).

Appendix A. Supplementary data

Supplementary data to this article can be found online at https://doi.org/10.1016/j.oregeorev.2025.106466.

Data availability

Data will be made available on request.

References

Amli, R., 1977. Carbonatites, a possible source of scandium as indicated by Sc mineralization in the Fen paralkaline complex, southern Norway. Economic Geology 72 (5), 855–859.

Anenburg, M., Broom-Fendley, S., Chen, W., 2021. Formation of rare earth deposits in carbonatites. Elements: an International Magazine of Mineralogy, Geochemistry, and Petrology 17 (5), 327–332.

Bai, G., Yuan, Z.X., Wu, C.Y., Zhang, Z.Q., Zheng, L.X., 1996. Demonstration on the geological features and genesis of the Bayan Obo ore deposit. Geological Publishing House, Beijing (in Chinese).

Bao, X.J., Wang, Z.J., Xi, L.J., Liu, J.B., Su, Z.F., Yang, T., Cheng, W., Zhou, D.B., 2022. Separation of Sc2O3 from Bayan Obo tailings through an innovative roasting method. Rare Metals 41, 1071–1076.

Beland, C.M., Williams-Jones, A.E., 2023. The genesis of a potential scandium ore deposit at Crater Lake. Canada. Chemical Geology 615, 121223.

Bruker, 2018, Mineral composition analysis using the M4 TornadoAmics. Lab report XRF 469 (Micro-XRF-Application-Note-XRF-469-Mineral-composition-analysis-using-M4-TORNADO-AMICS-EN-BRUKER.pdf).

Chassé, M., Griffin, W.L., O'Reilly, S.Y., Calas, G., 2016. Scandium speciation in a world-class lateritic deposit. Geochemical Perspectives Letters 3 (2), 105–114.

Chen, W., Liu, H.Y., Lu, J., Jiang, S.Y., Simonetti, A., Xu, C., Zhang, W., 2020. The formation of the ore-bearing dolomite marble from the giant Bayan Obo REE-Nb-Fe deposit, Inner Mongolia: Insights from micron-scale geochemical data. Mineralium Deposita 55, 131–146.

Chen, W., Ying, Y.C., Liu, J.J., Yang, F., Jiang, S.Y., 2024. The metallogenesis and genetic mechanism of the carbonatite-alkaline rock associated niobium and rare earth element deposits. Bulletin of Mineralogy, Petrology and Geochemistry 43 (1), 1–14. In Chinese with English abstract.

Čopjaková, R., Škoda, R., Galiová, M.V., Novák, M., Cempírek, J., 2015. Sc-and REE-rich tourmaline replaced by Sc-rich REE-bearing epidote-group mineral from the mixed (NYF+ LCT) Kracovice pegmatite (Moldanubian Zone, Czech Republic). American Mineralogist 100 (7), 1434–1451.

Critical Minerals Office, 2023. Australia's Critical Minerals List. Accessed 26 August 2023. https://www.industry.gov.au/publications/australias-critical-minerals-list.

Dietzel, C.A., Kristandt, T., Dahlgren, S., Giebel, R.J., Marks, M.A., Wenzel, T., Markl, G., 2019. Hydrothermal processes in the Fen alkaline-carbonatite complex, southern Norway. Ore Geology Reviews 111, 102969.

Donovan, J.J., Allaz, J.M., von der Handt, A., Seward, G.G.E., Neill, O., Goemann, K., Chouinard, J., Carpenter, P.K., 2021. Quantitative WDS compositional mapping using the electron microprobe. American Mineralogist V. 106, 11, 1717–1735.

Donovan, J.J., Tingle, T.N., 1996. An Improved Mean Atomic Number Correction for Quantitative Microanalysis. Journal of Microscopy 2 (1), 1–7.

Drew, L.J., Meng, Q., Sun, W., 1990. The Bayan Obo iron-rare-earth-niobium deposits, Inner Mongolia. China. Lithos 26 (1–2), 43–65.

Eby, G.N., 1973. Scandium geochemistry of the Oka carbonatite complex, Oka, Quebec. American Mineralogist: Journal of Earth and Planetary Materials 58 (9–10), 819–825.

Fan, H.R., Xie, Y.H., Wang, K.Y., Wilde, S.A., 2004. Methane-rich fluid inclusions in skarn near the giant REE–Nb–Fe deposit at Bayan Obo. Northern China. Ore Geology Reviews 25 (3–4), 301–309.

Fan, H.R., Hu, F.F., Yang, K.F., Wang, K.Y., 2006. Fluid unmixing/immiscibility as an ore-forming process in the giant REE-Nb-Fe deposit, Inner Mongolian, China: evidence from fluid inclusions. Journal of Geochemical Exploration 89 (1–3), 104–107.

Fan, H.R., Hu, F.F., Yang, K.F., Wang, K.Y., Liu, Y.S., 2009. Geochronology framework of late Paleozoic dioritic-granitic plutons I nthe Bayan Obo area, Inner Mongolia, and tectonic significance. Acta Petrologica Sinica 25 (11), 2933–2938 in Chinese with English abstract.

Fan, H.R., Hu, F.F., Yang, K.F., Pirajno, F., Liu, X., Wang, K.Y., 2014. Integrated U–Pb and Sm–Nd geochronology for a REE-rich carbonatite dyke at the giant Bayan Obo REE deposit, Northern China. Ore Geology Reviews 63, 510–519.

Fan, H.R., Yang, K.F., Hu, F.F., Liu, S., Wang, K.Y., 2016. The giant Bayan Obo REE-Nb-Fe deposit, China: controversy and ore genesis. Geoscience Frontiers 7 (3), 335–344.

Fan, H.R., Xu, Y., Yang, K.F., Zhang, J.E., Li, X.C., Zhang, L.L., She, H.D., Liu, S.L., Xu, X. W., Huang, S., Li, Q.L., Zhao, L., Li, X.H., Wu, F.Y., Zhai, M.G., Zhao, Y.G., Wang, Q. W., Yang, Z.F., Liu, Y., Yan, G.Y., Liu, Z.Q., Cui, F., Liu, F., 2022. Intrusive style, three-dimensional morphology of carbonatite and REE potential resources in the Bayan Obo giant deposit. Inner Mongolia. Acta Petrologica Sinica 38 (10), 2901–2919. In Chinese with English abstract.

European Commission, 2023. Critical raw materials Accessed 26 August 2023 https://single-market-economy.ec.europa.eu/sectors/raw-materials/areas-specific-interest/critical-raw-materials_en.

U.S. Geological Survey, 2024, Mineral commodity summaries 2024: U.S. Geological Survey, 212p., https://doi.org/ 10.3133/mcs2024.

Hagemann, H., Lucken, A., Bill, H., Gysler-Sanz, J., Stalder, H.A., 1990. Polarized Raman spectra of beryl and bazzite. Physics and Chemistry of Minerals 17, 395–401.

Halkoaho, T., Ahven, M., Rämö, O.T., Hokka, J., Huhma, H., 2020. Petrography, geochemistry, and geochronology of the Sc-enriched Kiviniemi ferrodiorite intrusion, eastern Finland. Mineralium Deposita 55, 1561–1580.

Hou, X., Yang, Z., Wang, Z., 2023. Occurrence State and Distribution Regularity of Key Metal Element Niobium in Bayan Obo Deposit. China. JOM 75 (7), 2753–2762. In Chinese with English abstract.

Hreus, S., Výravský, J., Cempírek, J., Breiter, K., Galiová, M.V., Krátký, O., Šešulka, V., Škoda, R., 2021. Scandium distribution in the world-class Li-Sn-W Cínovec greisen-type deposit: Result of a complex magmatic to hydrothermal evolution, implications for scandium valorization. Ore Geology Reviews 139, 104433.

Hu, F.F., Fan, H.R., Liu, S., Yang, K.F., Chen, F., 2009. Samarium-neodymium and rubidium-strontium isotopic dating of veined REE mineralization for the Bayan Obo REE-Nb-Fe deposit. Northern China. Resource Geology 59 (4), 407–414.

Ismail, R., Ciobanu, C.L., Cook, N.J., Teale, G.S., Giles, D., Mumm, A.S., Wade, B., 2014. Rare earths and other trace elements in minerals from skarn assemblages, Hillside iron oxide–copper–gold deposit, Yorke Peninsula, South Australia. Lithos 184–187, 456–477.

Kalashnikov, A.O., Yakovenchuk, V.N., Pakhomovsky, Y.A., Bazai, A.V., Sokharev, V.A., Konopleva, N.G., Mikhailova, J.A., Goryainov, P.M., Ivanyuk, G.Y., 2016. Scandium of the Kovdor baddeleyite–apatite–magnetite deposit (Murmansk Region, Russia): Mineralogy, spatial distribution, and potential resource. Ore Geology Reviews 72, 532–537.

Ke, C.H., Sun, S., Zhao, Y.G., Li, Y.K., Xv, Z.Y., Hao, M.Z., Li, R.P., Zhang, L., 2021. Ore-controlling structure and deep prospecting of the Bayan Obo large-sized REE-Nb-Fe ore deposit. Inner Mongolia. Geological Bulletin of China 40 (1), 95–109 in Chinese with English abstract.

Kolitsch, U., Kristiansen, R., Raade, G., Tillmanns, E., 2010. Heftetjernite, a new scandium mineral from the Heftetjern pegmatite, Tørdal. Norway. European Journal of Mineralogy 22 (2), 309–316.

Kuebler, C., Simonetti, A., Chen, W., Simonetti, S.S., 2020. Boron isotopic investigation of the Bayan Obo carbonatite complex: Insights into the source of mantle carbon and hydrothermal alteration. Chemical Geology 557, 119859.

Langan, T.J., Dorin, T., 2023. Scandium in Commercial Wrought Aluminum Alloys. Status and Prospects, Rare Earth Metals and Minerals Industries, pp. 359–389.

Lapin, A.V., Tolstov, A.V., Kulikova, I.M., 2016. Distribution of REE, Y, Sc, and Th in the unique complex rare-metal ores of the Tomtor deposit. Geochemistry International 54, 1061–1078.

Le Bas, M.J., Yang, X., Taylor, R.N., Spiro, B., Milton, J.A., Peishan, Z., 2007. New evidence from a calcite-dolomite carbonatite dyke for the magmatic origin of the massive Bayan Obo ore-bearing dolomite marble, Inner Mongolia, China[J]. Mineralogy and Petrology 90, 223–248.

Le Maitre, R.W., ed., 2002, Igneous Rocks: A Classification and Glossary of Terms: Cambridge, UK, Cambridge University Press, 236 p.

Li, X.C., Fan, H.R., Zeng, X., Yang, K.F., Yang, Z.F., Wang, Q.W., Li, H.T., 2021a. Identification of ~ 1.3 Ga hydrothermal zircon from the giant Bayan Obo REE deposit (China): Implication for dating geologically-complicated REE ore system. Ore Geology Reviews 138, 104405.

Li, X.C., Yang, K.F., Spandler, C., Fan, H.R., Zhou, M.F., Hao, J.L., Yang, Y.H., 2021b. The effect of fluid-aided modification on the Sm-Nd and Th-Pb geochronology of monazite and bastnäsite: Implication for resolving complex isotopic age data in REE ore systems. Geochimica et Cosmochimica Acta 300, 1–24.

Li, X.C., Fan, H.R., Su, J.H., Groves, D.I., Yang, K.F., Zhao, X.F., 2024. Giant Rare Earth Element Accumulation Related to Voluminous, Highly Evolved Carbonatite: A Microanalytical Study of Carbonate Minerals From the Bayan Obo Deposit. China. Economic Geology 119 (2), 373–393.

Li, Y.K., Ke, C.H., She, H.Q., Wang, D.H., Xu, C., Wang, A.J., Li, R.P., Peng, Z.D., Zhu, Z. Y., Yang, K.F., Chen, W., Zi, J.W., Song, W.L., Zhao, Y.G., Zhang, L., Yu, H., Guo, B., Zhou, S.Q., Yuan, X.Y., Liu, J.Y., 2023. Geology and mineralization of the Bayan Obo supergiant carbonatite-type REE-Nb-Fe deposit in Inner Mongolia, China: A review. China Geology 6 (4), 716–750.

Li, H.T., Yang, K.F., Gao, Y.P., Zhao, J., Yuan, X.Y., Li, X.C., Fan, H.R., 2022. Age and origin of the H9 member from the Bayan Obo Group: Implications for the genesis of the giant Bayan Obo Fe-Nb-REE deposit. China. Ore Geology Reviews 146, 104927.

Liu, S., Fan, H.R., Yang, K.F., Hu, F.F., Rusk, B., Liu, X., Li, X.C., Yang, Z.F., Wang, Q.W., Wang, K.Y., 2018. Fenitization in the giant Bayan Obo REE-Nb-Fe deposit: Implication for REE mineralization. Ore Geology Reviews 94, 290–309.
Liu, S., Fan, H.R., Santosh, M., Liu, X., Wang, Q.W., Butcher, A.R., 2023. Geological resources of scandium: a review from a Chinese perspective. International Geology Review 1–22.
Liu, Y.L., Yang, G., Chen, J.F., Du, A.D., Xie, Z., 2004. Re-Os dating of pyrite from giant Bayan Obo REE-Nb-Fe deposit. Chinese Science Bulletin 49, 2627–2631 in Chinese with English abstract.
Ma, S.F., 2012. Study on extraction technology of scandium from the Bayan Obo tailings. Inner Mongolia University (In Chinese with English Abstract).
Martin, L.H., Schmidt, M.W., Mattsson, H.B., Guenther, D., 2013. Element partitioning between immiscible carbonatite and silicate melts for dry and H2O-bearing systems at 1–3 GPa. Journal of Petrology 54 (11), 2301–2338.
Phoung, S., Williams, E., Gaustad, G., Gupta, A., 2023. Exploring global supply and demand of scandium oxide in 2030. Journal of Cleaner Production 401, 136673.
Pieczka, A., Kristiansen, R., Stachowicz, M., Dumańska-Słowik, M., Gołębiowska, B., Sęk, M.P., Nejbert, K., Kotowski, J., Marciniak-Maliszewska, B., Szuszkiewicz, A., Szełęg., E., Woźniak, K., 2024. Heflikite, ideally Ca2(Al2Sc)(Si2O7)(SiO4)O(OH), the first scandium epidote-supergroup mineral from Jordanów Śląski, Lower Silesia, Poland and from Heftetjern, Tørdal, Norway. Mineralogical Magazine, 1-16.
Pieczka, A., Stachowicz, M., Zelek-Pogudz, S., Gołębiowska, B., Sęk, M., Nejbert, K., Kotowski, J., Marciniak-Maliszewska, B., Szuszkiewicz, A., Szełęg, E., Stadnicka, K. M., Woźniak, k., 2024b. Scandio-winchite, ideally□(NaCa)(Mg4Sc)(Si8O22)(OH) 2: The first Sc-dominant amphibole-supergroup mineral from Jordanów Śląski, Lower Silesia, southwestern Poland. American Mineralogist, 109(5), 940-948.
Pieczka, A., Stachowicz, M., Zelek-Pogudz, S., Gołębiowska, B., Sęk, M., Nejbert, K., Kotowski, J., Marciniak-Maliszewska, B., Szuszkiewicz, A., Szełęg, E., Stadnicka, K. M., Woźniak, k., 2024c. Scandian actinolite from Jordanów Śląski, Lower Silesia, Poland: Compositional evolution, crystal structure, and genetic implications. American Mineralogist, 109(1), 174-183.
Pouchou, J.L., Pichoir, F., 1991. Quantitative Analysis of Homogeneous or Stratified Microvolumes Applying the Model "PAP". In: Heinrich, K.F.J., Newbury, D.E. (Eds.), Electron Probe Quantification. Plenum Press, New York, pp. 31–75.
Ren, Y., Zhan, Y., Zhang, Z., 1994. Study of heat events of ore-forming Bayan Obo deposit. Acta Geoscientica Sinica 30–31, 95–101 in Chinese with English abstract.
Ren, Y., Yang, X., Yang, X., Ling, M., Liu, Y., 2023. Mineralogical study on the distribution regularity of niobium in various types of ores in the giant Bayan Obo Fe-REE-Nb deposit. Ore Geology Reviews 105602.
Samon, M.I., Chassé, M., 2016. Scandium. Springer International Publishing Switzerland, William M. White. Encyclopedia of Geochemistry, pp. 1–4.
Shannon, R.D., 1976. Revised effective ionic radii and systematic studies of interatomic distances in halides and chalcogenides. Acta Crystallographica Section a: Crystal Physics, Diffraction, Theoretical and General Crystallography 32 (5), 751–767.
Shao, D., Song, J., Du, X., Deng, Y., Xue, Z., Yu, H., Qi, T., 2023. Leaching characteristics and kinetics of scandium from Sc-concentrate of Bayan Obo rare earth tailings in sulfuric acid solution. Journal of Environmental Chemical Engineering 11 (5), 111037.
Shchekina, T.I., Gramenitskii, E.N., 2008. Geochemistry of Sc in the magmatic process: Experimental evidence. Geochemistry International 46 (4), 351–366.
She, H.D., Fan, H.R., Yang, K.F., Li, X.C., Yang, Z.F., Wang, Q.W., Zhang, L.F., Wang, Z.J., 2021. Complex, multi-stage mineralization processes in the giant Bayan Obo REE-Nb-Fe deposit. China. Ore Geology Reviews 139, 104461.
She, H.D., Fan, H.R., Santosh, M., Li, X.C., Yang, K.F., Wang, Q.W., Wei, W., Liu, Y.J., Liu, S., Liu, S.L., 2023. Paleozoic remelting of carbonatite in Bayan Obo (China): Further insights into the formation of a giant REE deposit. Gondwana Research 119, 172–185.
Shimazaki, H., Yang, Z., Miyawaki, R., Shigeoka, M., 2008. Scandium-Bearing Minerals in the Bayan Obo Nb-REE-Fe Deposit, Inner Mongolia. China. Resource Geology 58 (1), 80–86.
Siegfried, P., Wall, F., Moore, K., 2018. In search of the forgotten rare earth. Geological Society of London.
Smith, M.P., Campbell, L.S., Kynicky, J., 2015. A review of the genesis of the world class Bayan Obo Fe–REE–Nb deposits, Inner Mongolia, China: Multistage processes and outstanding questions. Ore Geology Reviews 64, 459–476.
Steffenssen, G., Müller, A., Munnik, F., Friis, H., Erambert, M., Kristoffersen, M., Rosing-Schow, N., 2020. Unusual scandium enrichments of the Tørdal pegmatites, south Norway. Part I: Garnet as Sc exploration pathfinder. Ore Geology Reviews 126, 103729.
Stokkeland, K., 2016. Formation of thortveitite and garnet chemistry in the Evje-Iveland pegmatite field (Master's thesis).
Tang, H., Liu, Y., Song, W., 2021. Igneous genesis of the Bayan Obo REE–Nb–Fe deposit: New petrographical and structural evidence from the H1–H9 cross-section and deep-drilling exploration. Ore Geology Reviews 138, 104397.
Tolstov, A.V., Gunin, A.P., 2001. Comprehensive assessment of the Tomtor deposit. Vestnik VGU 11, 144–160.
Verbaan, N., Johnson, M., Grammatikopoulos, T., Larochelle, E., Honan, S., Smith, K., Sixberry, R., 2018. A process flowsheet for the extraction of niobium, titanium, and scandium from Niocorp's Elk Creek Deposit. In: Extraction 2018: Proceedings of the First Global Conference on Extractive Metallurgy, pp. 2523–2539.
Verplanck, P.L., Farmer, G.L., Kettler, R.M., Lowers, H.A., Johnson, C.A., Koenig, A.E., Blessington, M.J., 2022. Petrogenesis and rare earth element mineralization of the Elk Creek carbonatite, Nebraska, USA. Ore Geology Reviews 146, 104953.
Wang, Z., Li, M.Y.H., Liu, Z.R.R., Zhou, M.F., 2021. Scandium: Ore deposits, the pivotal role of magmatic enrichment and future exploration. Ore Geology Reviews 128, 103906.
Wang, J., Williams-Jones, A.E., Timofeev, A., Liu, J., Yuan, S., 2022a. An experimental investigation of the solubility and speciation of scandium in fluoride-bearing aqueous liquids at temperatures up to 250° C. Geochimica et Cosmochimica Acta 330, 67–79.
Wang, J., Williams-Jones, A.E., Timofeev, A., Zhang, X., Liu, J., Yuan, S., 2023. The role of scandium chloride and hydroxide complexes in the formation of scandium deposits: insights from experiments and modeling. Economic Geology 118 (8), 1995–2004.
Wang, J., Li, L., Santosh, M., Yan, G.Y., Shen, J.F., Yuan, M.W., Alam, M., Li, S.R., 2024. Multistage ore formation in the world's largest REE-Nb-Fe deposit of Bayan Obo. New insights and implications. Ore Geology Reviews, North China Craton, p. 105817.
Wang, L., Wang, P., Chen, W.Q., Wang, Q.Q., Lu, H.S., 2020. Environmental impacts of scandium oxide production from rare earths tailings of Bayan Obo Mine. Journal of Cleaner Production 270, 122464.
Wang, Z.C., Zhou, M.F., Li, M.Y.H., Robinson, P.T., Harlov, D.E., 2022b. Kinetic controls on Sc distribution in diopside and geochemical behavior of Sc in magmatic systems. Geochimica et Cosmochimica Acta 325, 316–332.
Wei, C.W., Deng, M., Xu, C., Chakhmouradian, A.R., Smith, M.P., Kynicky, J., Song, W.L., Chen, W., Fu, B., 2022. Mineralization of the Bayan Obo rare earth element deposit by recrystallization and Decarbonation. Economic Geology 117 (6), 1327–1338.
Williams-Jones, A.E., Vasyukova, O.V., 2018. The economic geology of scandium, the runt of the rare earth element litter. Economic Geology 113 (4), 973–988.
Yang, K., Fan, H., Pirajno, F., Li, X., 2019. The Bayan Obo (China) giant REE accumulation conundrum elucidated by intense magmatic differentiation of carbonatite. Geology 47 (12), 1198–1202.
Yang, K.F., Fan, H.R., Pirajno, F., Liu, X., 2023a. Magnesium isotope fractionation in differentiation of mafic-alkaline-carbonatitic magma and Fe-P-REE-rich melt at Bayan Obo. China, Ore Geology Reviews, p. 105466.
Yang, K.F., Fan, H.R., Qiu, Z.J., Li, X.C., She, H.D., Liu, S.L., Li, H.T., Zhang, L.F., 2023b. Spatial distribution pattern of ore-forming elements in the Bayan Obo deposit and exploration implications. Acta Petrologica Sinica 39 (10), 2895–2909. In Chinese with English abstract.
Yang, X., Lai, X., Pirajno, F., Liu, Y., Mingxing, L., Sun, W., 2017. Genesis of the Bayan Obo Fe-REE-Nb formation in Inner Mongolia, north China craton: a perspective review. Precambrian Research 288, 39–71.
Yang, X.M., Yang, X.Y., Fan, H.R., Guo, F., Zhang, Z.F., Zhang, P.S., 2000. Rare earth element geochemistry of the Heicynian granite complex at Bayan Obo, Inner Mongolia, China. Chinese Rare Earths 21, 1–7. In Chinese with English abstract.
Yang, B., Yang, L., Meng, W., 2022. Application of Electron Probe Microanalyzer in Exploring the Occurrence Characteristics of Scandium in Different Minerals of the Bayan Obo Deposit. Rock and Mineral Analysis 41 (2), 185–198.
Yaxley, G.M., Anenburg, M., Tappe, S., Decree, S., Guzmics, T., 2022. Carbonatites: classification, sources, evolution, and emplacement. Annual Review of Earth and Planetary Sciences 50, 261–293.
Yu, Y., Li, Y., Liu, Y., Ling, X.X., Wu, L.G., Yang, L., Yang, L., Yang, B., Zhao, Y.G., Li, X. H., 2024. Three-stage niobium mineralization at Bayan Obo. China. National Science Review 11 (4), nwae063.
Zhan, Y.X., Li, X.C., Wu, B., Yang, K.F., Fan, H.R., Li, X.H., 2023. The occurrence and genesis of HREE-rich minerals from the giant Bayan Obo deposit. China, Ore Geology Reviews, p. 105438.
Zhang, B., Xue, X., Huang, X., Yang, H., Chen, G., 2019. Study on recycling and leaching valuable elements from Bayan Obo tailings. Metallurgical Research & Technology 116 (1), 114.
Zhang, S.H., Zhao, Y., Li, Q.L., Hu, Z.C., Chen, Z.Y., 2017a. First identification of baddeleyite related/linked to contact metamorphism from carbonatites in the world's largest REE deposit, Bayan Obo in North China Craton. Lithos 284, 654–665.
Zhang, S.H., Zhao, Y., Liu, Y., 2017b. A precise zircon Th-Pb age of carbonatite sills from the world's largest Bayan Obo deposit: Implications for timing and genesis of REE-Nb mineralization. Precambrian Research 291, 202–219.
Zhou, M.F., Li, M.Y.H., Wang, Z., Li, X.C., Liu, J., 2020. The genesis of regolith-hosted rare earth element and scandium deposits: Current understanding and outlook to future prospecting. Chinese Science Bulletin 65 (33), 3809–3824.
Zhou, M.F., Wang, Z.C., Zhao, W.W., Qi, L., Zhao, Z., Zhou, J., Huang, Z., Chen, W.T., 2022. A reconnaissance study of potentially important scandium deposits associated with carbonatite and alkaline igneous complexes of the Permian Emeishan Large Igneous Province, SW China. Journal of Asian Earth Sciences 236, 105309.
Zhu, Z., Wang, D., Li, Y., Ke, C., Yu, H., Chen, Z., She, H., Wang, R., Hu, H., Zhao, Y., Guo, B., 2024. Detail mineralogical study and geochronological framework of Bayan Obo (China) Nb mineralization recorded by in situ U-Pb dating of columbite. Ore Geology Reviews 105874.
Zou, H.B., 2014. Error propagation. In: Holland H.D. and Turekian K.K. (eds.) Treatise on Geochemistry (Second Edition), 15, 33-42.